

B-FROST: B-Fields and Star Formation across Scales with TRAO CO Abundances, Dynamics and Relative Orientations in the Translucent High Latitude Cloud MBM12

J.M. Vorster¹, J. Montillaud², M. Juvela¹, E. Falgarone¹⁸, J. Oers³, E. Mannfors¹, D. Alina⁴, Q. Gu^{5,6}, H. Kang^{7,8},
C.W. Lee^{7,9}, S. Li^{5,6}, T. Liu¹⁰, K. Pattle¹¹, V.-M. Pelkonen^{12,13}, I. Ristorcelli³, A. Zavagno^{15,16}, and L. V. Tóth^{14,17}

¹ Department of Physics, University of Helsinki, Finland
e-mail: jakobus.vorster@helsinki.fi

² Institut UTINAM – UMR 6213 – CNRS – Univ. Bourgogne Franche Comté, OSU THETA, 41bis avenue de l’Observatoire, 25000
Besançon, France

³ IRAP, Université de Toulouse, CNRS, Toulouse, France

⁴ Physics Department, School of Sciences and Humanities, Nazarbayev University, Astana, Kazakhstan.

⁵ School of Astronomy and Space Science, Nanjing University, Nanjing, People’s Republic of China

⁶ Key Laboratory of Modern Astronomy and Astrophysics (Nanjing), Ministry of Education, Nanjing, People’s Republic of China

⁷ Korea Astronomy and Space Science Institute, Daejeon, Republic of Korea

⁸ Astronomy Program, Department of Physics and Astronomy, Seoul National University, Seoul, Korea

⁹ University of Science and Technology, Korea (UST), Daejeon, Republic of Korea

¹⁰ Shanghai Astronomical Observatory, Chinese Academy of Sciences, Shanghai, People’s Republic of China

¹¹ Department of Physics and Astronomy, University College London, London, United Kingdom

¹² Institut de Ciències del Cosmos, Universitat de Barcelona, Barcelona, Spain.

¹³ INAF - IAPS, via Fosso del Cavaliere, 100, Roma, Italy

¹⁴ Institute of Physics and Astronomy, ELTE Eötvös Loránd University, Budapest, Hungary

¹⁵ Aix Marseille Univ, CNRS, CNES, LAM, Marseille, France

¹⁶ Institut Universitaire de France, 1 rue Descartes, Paris

¹⁷ Institute of Physics, University of Debrecen, Hungary

¹⁸ LPENS, Ecole Normale Supérieure, Université PSL, CNRS, Sorbonne Université, Université de Paris, France

Received February 26, 2026; accepted May 18, 2026

ABSTRACT

Context. On average, in our Galaxy, the star formation efficiency (SFE) is of the order of a few percent, lower than theoretical predictions. Detailed observational studies of individual molecular clouds may highlight the contributing factors to the low galactic SFE.

Aims. We investigated the high-latitude molecular cloud MBM12 as part of the B-fields and star formation across scales (B-FROST) survey with the Taeduk Radio Astronomical Observatory (TRAO) to assess why star formation activity in MBM12 is low.

Methods. We estimated $N(\text{H}_2)$ with *Herschel* dust emission and a dust opacity κ_v , derived from near-infrared extinction, 21 cm HI column densities and far-infrared emission. With ^{12}CO and ^{13}CO ($J = 1 - 0$) line observations, covering an area of $2.5^\circ \times 3^\circ$ at $48''$ resolution we mapped the CO column density $N(\text{CO})$, CO-to- H_2 factor $X(\text{CO})$, and abundance $[\text{CO}/\text{H}_2]$. We estimated the multi-scale virial parameter α_{vir} and constructed mass-size scaling laws of hierarchical structures with dendrograms. We computed the relative orientation between column density structures and magnetic fields using *Planck* observations of dust polarisation.

Results. We identify four main regions based on velocities with H_2 column densities ranging from $2 \times 10^{20} \text{ cm}^{-2} - 1.3 \times 10^{22} \text{ cm}^{-2}$. The CO integrated line intensity, $W(\text{CO})$, increases linearly with $N(\text{H}_2)$ providing an average $X(\text{CO})$ factor close to the galactic average. At low $N(\text{H}_2)$, $X(\text{CO})$ varies below X_{Gal} due to the fall-off of collisional de-excitation in low density gas, and above X_{Gal} due to the drop of CO abundances in poorly shielded cloud edges. The hierarchical structures follow a broken power law mass-size relation $M = AR^\alpha$. The values of α_{vir} ranged from 3 – 60, with the smallest values at 0.1 pc scales. The mass-size relations for the structures with the lowest α_{vir} have scaling factors A three times larger than those of high α_{vir} structures, indicating external pressure one order of magnitude larger than the former. We found a transition of parallel to perpendicular between column density structures and magnetic field orientations at $N(\text{H}_2) = 4.5 \times 10^{21} \text{ cm}^{-2}$.

Conclusions. We provide the first integrated chemical, dynamical, and magnetic field analysis of MBM12. Further investigation into the scale dependence of the mass-size relation and virial parameter can highlight the role of external pressure in regulating the star-formation efficiency.

Key words. Methods: observational – ISM: clouds – ISM: individual objects: MBM12 – ISM: abundances – ISM: kinematics and dynamics – ISM: magnetic fields

1. Introduction

Molecular clouds (MCs) are among the densest and coldest large-scale structures in the interstellar medium (ISM) and the sites of star formation in galaxies. They evolve under the combined effects of self-gravity, turbulence, magnetic fields, radiation and stellar feedback (Hennebelle & Falgarone 2012). The chemical evolution of MCs is closely linked to their dynamics due to comparable dynamical and chemical timescales (Dobbs et al. 2014; Chevance et al. 2023). The most commonly used tracers for large scale (> 1 pc) molecular cloud properties are carbon monoxide (CO) line emission, near-infrared (NIR) extinction, and far-infrared (FIR) dust emission, each offering complementary insights. Galactic surveys of ^{12}CO ($J = 1 - 0$) line emission have been used for over forty years to estimate MC masses, sizes, surface densities, densities and velocity dispersions. These measurements underpin many of the classic MC scaling relations (Wilson et al. 1970; Solomon et al. 1987; Dame et al. 2001; Roman-Duval et al. 2010; Miville-Deschênes et al. 2017).

Near-infrared extinction is another dust-based tracer of MC structure, though the consequent column densities depends on the assumed extinction law, but is independent of dust temperature variations along the line of sight (Lada et al. 1994; Alves et al. 2001; Hasenberger et al. 2018). With the all-sky 2MASS survey, it is possible to produce $\sim 5'$ resolution extinction maps for most of the sky (Skrutskie et al. 1997; Lombardi & Alves 2001; Lombardi 2009; Juvela & Montillaud 2016). The achievable resolution and dynamic range of column densities from NIR extinction are limited by stellar density.

Far-infrared dust emission is not limited by background stellar density. The *Planck* satellite observed the entire sky at $5'$ resolution (e.g. Planck Collaboration et al. 2014a), while the *Herschel* satellite allowed sub-arcmin resolution and two-order-of-magnitude range in column density (Juvela et al. 2010; André et al. 2010; Juvela et al. 2011). Polarized dust emission also enables measurements of magnetic field orientation (Pattle et al. 2023).

Each tracer presents unique advantages and limitations. CO line emission can probe gas dynamics and chemistry, but transitions between sub-thermal, thermal, optically thick, and self-absorbing regimes complicate mass and column density estimates (e.g. Goodman et al. 2009). Extinction is among the most reliable tracers of hydrogen column density $N(\text{H})$ for a constant dust to gas ratio, though the extinction law R_V may vary and the attainable resolution is limited. FIR dust emission offers high resolution and dynamic range but depends on variable dust opacities and requires high-altitude or space-based observations. Magnetic field measurements are constrained by sensitivity and resolution, but they provide critical insight into the magnetohydrodynamic (MHD) processes shaping MCs (Pattle et al. 2023). A key limitation of all dust-based tracers is their inability to resolve structures along the line of sight at high resolution (recent 3D extinction maps are addressing this problem at scales > 10 pc, Zucker et al. 2023).

With the advent of wide-field surveys and improved resolution, it is now possible to combine multiple tracers across large MC samples to test abundance variations, excitation conditions, and structural properties (Lombardi et al. 2006; Goodman et al. 2009; Pineda et al. 2010; Kong et al. 2015; Pety et al. 2017; Lewis et al. 2021). However, such multi-tracer analyses are rarely conducted systematically across large samples, with a few exceptions (e.g. Lewis et al. 2022; Santa-Maria et al. 2023). The B-Fields and star Formation across Scales with TRAO (B-

FROST) survey has completed over 2500 hours of ^{12}CO and ^{13}CO ($J = 1 - 0$) observations, covering nine star-forming regions across 90 square degrees (Montillaud et al., in prep). B-FROST aims to characterize the relationship between CO chemistry, multi-scale dynamics, and magnetic fields across a diverse set of environments: from high-mass star-forming regions (Monoceros OB1, W40), and feedback-dominated regions (two fields in the λ Orionis ring), to low-mass isolated clouds (MBM12, L183), and compact globules (G110-13, L1780). These sources are at distances of 100 to 700 pc, corresponding to spatial resolutions from ~ 0.03 pc to ~ 0.15 pc respectively.

In single-tracer surveys, environmental diversity can be a weakness, introducing unknown systematics. However, because B-FROST explicitly seeks to understand how CO chemistry and dynamics interact with magnetic fields across environments, this diversity becomes a strength. Therefore, conducting in-depth studies across diverse environments allows us to identify both general trends in star-forming regions and environment-specific variations.

The most basic CO observable is the line area $W(\text{CO}) = \sum_{\text{chan}} T_b \Delta\nu$, with T_b the brightness temperature and $\Delta\nu$ the channel width. The line area is related to the molecular hydrogen column density $N(\text{H}_2)$ through $X(\text{CO}) = N(\text{H}_2)/W(\text{CO})$. For ^{12}CO this factor has a Galactic average value of $X_{\text{Gal}} = 2 \times 10^{20} \text{ cm}^{-2} (\text{K km s}^{-1})^{-1}$ (Bolatto et al. 2013). This conversion factor is essential in extragalactic studies, where high resolution CO observations are often the only way to trace mass (e.g. Sun et al. 2018; Schinnerer & Leroy 2024; Leroy et al. 2025). The $X(\text{CO})$ factor is normally calculated as a means to an end (to convert CO intensity to mass), but it is rarely used as a tracer of physical properties in and of itself. It is well known that it varies on intra-cloud scales (e.g. Kong et al. 2015; Lewis et al. 2022). By definition, it is the H_2 column density per CO photon, and is therefore connected to processes of H_2 and CO abundance variation, as well as CO line excitation and radiative transfer.

The CO column density $N(\text{CO})$ is another fundamental measure. With various assumptions, one can estimate the total CO content of a molecular cloud (see Sect. 3.2). When combined with independent measures of $N(\text{H}_2)$, one can get the projected CO abundance $[\text{CO}/\text{H}_2]$. The CO abundance has been used to detect CO freezing onto dust grains in the coldest and densest parts of molecular clouds (Pineda et al. 2010; Lewis et al. 2021). Although CO chemistry has been studied for decades, the relative role of UV-driven CO chemistry with dynamically induced chemistry is still an open question (van Dishoeck & Black 1988; Hennebelle & Falgarone 2012). Photodissociation region models of turbulent molecular clouds fail to reproduce observed abundances in translucent gas (Levrier et al. 2012). Further, high resolution maps of abundance have not yet been utilized on a large scale.

Complementary to environmental characteristics of MCs are their dynamics. Self-gravity competes with internal turbulence, magnetic tension, magnetic pressure gradients and stellar feedback (Chevance et al. 2023). Molecular clouds are characterized by self-gravitating filamentary structures (e.g. André et al. 2010). There is some disagreement about whether the dominant mechanism for MC structure is self-gravity or supersonic turbulence (Vázquez-Semadeni et al. 2019; Padoan et al. 2020). There is a number of statistical tests that can be run on a position-position-velocity (PPV) cube, but projection effects and molecular abundances make direct comparison with simulations difficult (e.g. the tools in Koch et al. 2019). One controversial but easy to calculate measure of gravitational binding is the virial parameter α_{vir} , where super- and sub-virial are relative to $\alpha_{\text{vir}} = 2$

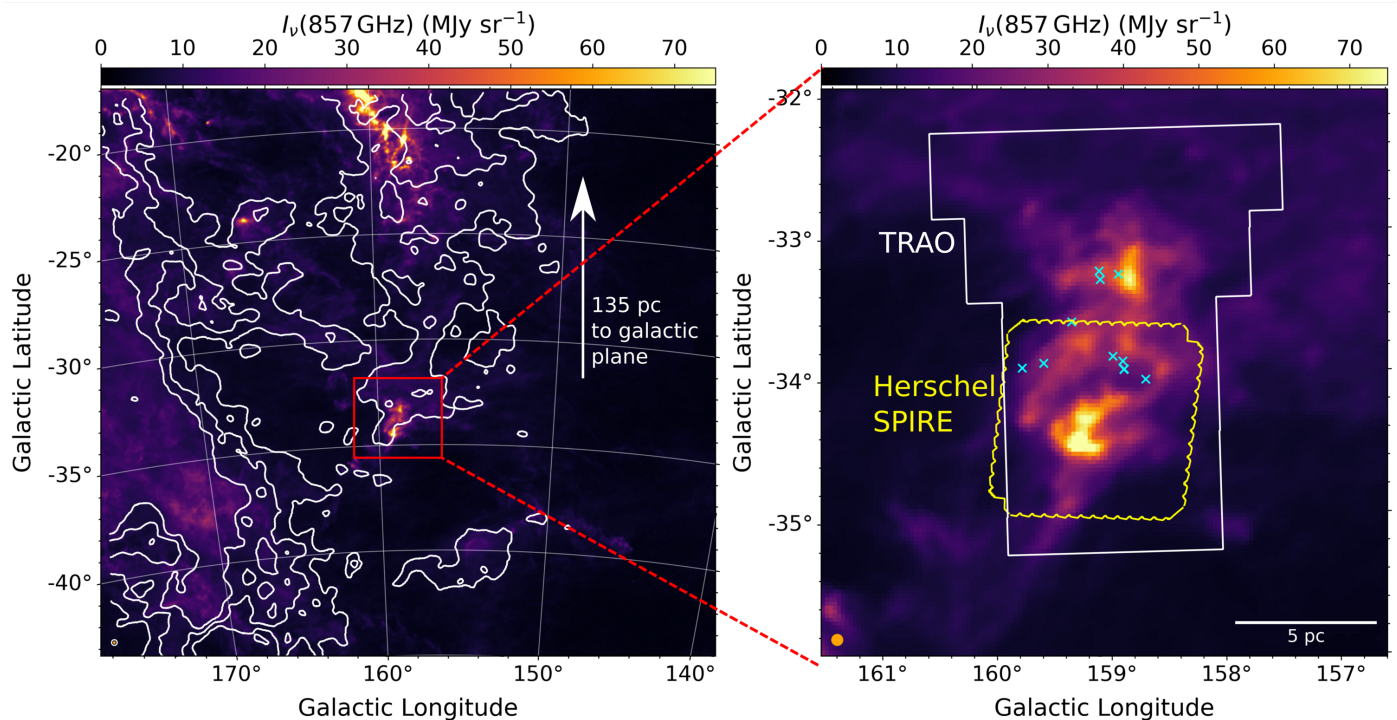


Fig. 1. Left: Position of MBM12 relative to the galactic disk. The colour scale shows *Planck* 857 GHz dust continuum and the contours are neutral hydrogen column density with contours at levels $[1.0, 1.2, 1.4] \times 10^{21} \text{ cm}^{-2}$ from the HI4PI all sky survey (HI4PI Collaboration et al. 2016). The beam sizes of *Planck* 857 GHz (orange) and HI4PI (white) are shown in the bottom left. Assuming a distance of 252 pc to MBM12 and a solar height of 20 pc above the galactic plane, the distance of MBM12 from the galactic plane is shown in white. Right: Zoom-in of MBM12 with the positions of T Tauri stars from Meeus et al. (2009) shown with cyan [x] markers. The observing field of view of the TRAO and *Herschel* SPIRE observations used in this work are shown in white and yellow respectively. A distance scale is shown in the bottom right.

(Bertoldi & McKee 1992), where

$$\alpha_{\text{vir}} = \frac{5\sigma_{\text{v,st}}^2 R_{\text{st}}}{GM_{\text{st}}}, \quad (1)$$

with $\sigma_{\text{v,st}}$ the 1D velocity dispersion of the structure, R_{st} the size, G the gravitational constant and M_{st} the mass of the structure (Bertoldi & McKee 1992; Kauffmann et al. 2013). The case of $\alpha_{\text{vir}} < 2$ does not necessarily imply "bound" and $\alpha_{\text{vir}} > 2$ "unbound" (see the brief discussion in App. F). Yet, it can be useful when used in conjunction with other tracers and paired with a physically motivated definition of a cloud. The dendrogram algorithm by Rosolowsky et al. (2008) is a natural way to segment PPV cubes into hierarchical structures. Many analyses utilize the highest levels of dendrogram structures (e.g. Friesen & Jarvis 2024), yet only a few utilize the full multi-scale hierarchy produced by the dendrogram algorithm (Oakes et al. 2025). Tracing the scale dependence of α_{vir} within a MC structure may yield additional insights into its stability.

Magnetic fields should not be ignored, as they increase in strength with density (Crutcher et al. 2010; Pattle et al. 2023). There has been a lot of work done mapping B-fields across scales in molecular clouds (Arzoumanian et al. 2021; Hwang et al. 2025). In many MCs, magnetic fields transition from being parallel to column density structures at low column densities to perpendicular at high column densities, suggesting they influence cloud evolution (Soler et al. 2013; Soler 2019). Highly magnetized gas has preferential motion along field lines, leading to a perpendicular arrangement at the strong field, high density limit (Soler et al. 2017; Suin et al. 2025). Algorithms such as FiLDReaMS allow a multi-scale consideration of B-field to col-

umn density relative orientations (Carrière et al. 2022a,b, Oers et al. submitted). Magnetic field studies are not often paired with CO virial analyses, but they may complement one another. Virial analysis with CO typically ignores magnetic fields, and relative orientation analysis cannot separate components along the line of sight.

The source we investigate as part of the B-FROST survey in this paper is the high-latitude molecular cloud MBM12 (Fig. 1). MBM12 has an estimated age of 2_{-1}^{+3} Myr, and contains about a dozen T Tauri stars (Luhman 2001; Hogerheijde et al. 2002; Meeus et al. 2009; Kim et al. 2012). It is at a distance of $252_{-6}^{+4} \pm 12$ pc (Zucker et al. 2019), and is a well-studied molecular cloud from the MBM catalogue (Magnani et al. 1985). Analysis of large-scale CO mapping assumed a distance of 65 pc, and concluded from a virial analysis that MBM12 is dispersing or pressure-bound (Pound et al. 1990). Analysis of ammonia mapping of MBM12 concluded that it is not forming stars (Gómez et al. 2000). It was also studied as part of the Galactic Cold Cores *Herschel* programme, with an estimated mass of $1.2 \times 10^3 M_{\odot}$ (Montillaud et al. 2015). A follow-up IRAM 30-m survey of one of the cores found rich prestellar chemistry, but did not detect deuterium or oxygen-bearing species, suggesting a quiescent core, or one at the early stages of star formation (Zhou et al. 2022). Virial analysis of a recent CO survey found $\alpha_{\text{vir}} > 30$ for most cores in the cloud (Xu et al. 2021). However, Moriarty-Schieven et al. (1997) used CO and HI observations to show that MBM12 might be pressure compressed at its southern end. So although most studies imply that MBM12 has finished forming stars and is dispersing into the environment, it may contain gas at the onset of triggered star formation.

As part of the B-FROST survey, we present an in-depth case study of MBM12. In this work, we aim to test whether MBM12 shows signs of gravitational instability despite previous indications of dispersal. We also assess how CO chemistry varies across the cloud, and whether magnetic field orientation correlates with structural or dynamical features. By combining ^{12}CO and ^{13}CO line emission with *Herschel* dust continuum data, we derive spatially resolved estimates of $X(\text{CO})$, $N(\text{CO})$, $[\text{CO}/\text{H}_2]$ and α_{vir} across 0.05 - 1 pc scales. MBM12's high-latitude environment allows us to explore the role of magnetic fields and the interplay between CO chemistry and gravitational stability in a relatively pristine setting. In Section 2 we introduce the data from TRAO, *Herschel* and *Planck* observations. Then we describe our methods for estimates of H_2 column density (Sect. 3.1), CO column density (Sect. 3.2), virial parameters (Sect. 3.3), and histogram of relative orientations (HROs, Sect. 3.4). In Section 4.1 we analyze the spatial distribution and probability density functions (PDFs) of $N(\text{H}_2)$, $N(\text{CO})$, $X(\text{CO})$ and $[\text{CO}/\text{H}_2]$ and compare these quantities against each other. We then look at multi-scale virial parameters (Sect. 4.2) and the histogram of relative orientation for MBM12 (Sect. 4.3). We discuss our findings in Section 5.

2. Observations

2.1. TRAO observations

The B-FROST survey observed MBM12 (l,b) = (159°00'00", -34°00'00") for 288 hours with the TRAO, operated by the Korean Astronomy and Space Science Institute (KASI)¹. More details on the observations, data reduction and data quality are found in Montillaud et al. (in prep). We observed the ^{12}CO ($J = 1 - 0$) and the ^{13}CO ($J = 1 - 0$) molecular lines simultaneously in on-the-fly mode with a spectral resolution of 0.2 km s⁻¹. The angular resolution was between 46" and 48" for 110 GHz - 115 GHz, and pointing accuracy was better than 10" (Jeong et al. 2019). We resampled all data to a grid resolution of 44". MBM12 was mapped by scanning 0.6° × 0.6° tiles in orthogonal l and b directions. The average system temperature was 300 K and 660 K at 110 GHz and 115 GHz respectively, but we repeated the scans until the desired noise level was reached. The final map size was 2.5° × 3°. The tiles were gridded and averaged with the GILDAS CLASS² software to make a single spectral cube for each line. We achieved a T_{A}^* sensitivity of $\sigma_{^{12}\text{CO}} = 0.28$ K and $\sigma_{^{13}\text{CO}} = 0.13$ K for most of the tiles, although some areas had a higher noise level. We converted the antenna temperature T_{A}^* to main beam temperature T_{mb} by dividing the antenna temperature by $\eta_{\text{eff}} = 0.51$ at 115 GHz and $\eta_{\text{eff}} = 0.54$ at 110 GHz.

2.2. *Herschel* and *Planck* observations

MBM12 was observed with the *Herschel* Space Observatory Spectral and Photometric Imaging REceiver (SPIRE, Griffin et al. 2010) at 250 μm , 350 μm and 500 μm as part of the Galactic Cold Cores open time programme (Juvela et al. 2010). We retrieved the MBM12 maps from the *Herschel* archive. The resolutions for these maps are about 18", 25", and 37". The relative calibration accuracies of the *Herschel* SPIRE surface brightness maps are expected to be better than 4% (Bendo et al.

2013)³. We also used the *Planck* 353 GHz full mission data, which are available as part of the Product Release 2018 in the *Planck* Legacy Archive⁴, observed with the *Planck* High Frequency Instrument (HFI, Lamarre et al. 2010). We extracted from the all-sky *Planck* data 2° × 2° maps of the Stokes total intensity I and the Q and U parameters, which correspond to the linear polarisation components, and their uncertainties at 353 GHz centred on the *Herschel* maps of MBM12. We smoothed the *Planck* maps from an angular resolution of 4.7' to 7' to improve the signal-to-noise ratio. Appendix A describes our estimates of the polarisation angles.

3. Methods

3.1. H_2 column density from dust emission

The *Herschel* SPIRE 250 μm , 350 μm and 500 μm maps were fit with modified black body (MBB) functions. Maps were colour corrected, background subtracted and convolved to an angular resolution of 40". The background subtraction was done by subtracting the average surface brightness of low-emission region centred on $(\alpha, \delta) = (2^{\text{h}}53^{\text{m}}56^{\text{s}}, +19^{\circ}19'17'')$ with a radius of 4' from each map. If the dust emission is optically thin the intensity I_{ν} can be written as:

$$I_{\nu} \approx B_{\nu}(T_{\text{dust}})\tau_{\nu}, \quad (2)$$

with $B_{\nu}(T_{\text{dust}})$ a black body intensity with dust temperature T_{dust} . The values of τ_{ν} and T_{dust} for each pixel, as well as their uncertainties, were estimated with Markov Chain Monte Carlo (MCMC) runs as in Juvela et al. (2015). The H_2 column density, $N(\text{H}_2)$, can then be estimated from:

$$N(\text{H}_2) = \frac{\tau_{\nu}}{\kappa_{\nu}\mu_{\text{H}_2}m_{\text{p}}}, \quad (3)$$

where τ_{ν} is the dust optical depth at a frequency ν , κ_{ν} the dust opacity in cm² g⁻¹ assuming a dust-to-gas ratio of 100, m_{p} the proton mass, and the molecular mass per H_2 molecule $\mu_{\text{H}_2} = 2.74$ (e.g. Heiderman et al. 2010). The opacity is known to vary by a factor of three between the dense and diffuse ISM (Planck Collaboration et al. 2014a; Ysard et al. 2015; Juvela et al. 2015). Our source, MBM12, is a high-latitude cloud, so assuming a literature value of κ_0 for the partly translucent ISM may be unreliable. Therefore, we explored empirical calibration of κ_{ν} . Calibration of κ_{ν} to use with FIR emission requires a reference column density estimate from an independent tracer. We calibrated the 250 μm (1200 GHz) optical depth τ_{1200} against the K-band extinction A_{K} (Lombardi et al. 2014; Lewis et al. 2022). For a Cardelli et al. (1989) extinction curve, $R_{\text{V}} = 3.1$, and an extinction to atomic hydrogen column density conversion factor $\beta_{\text{K}} \equiv N(\text{H})/A_{\text{K}} = 1.67 \times 10^{22}$ cm⁻² mag⁻¹, the dust opacity for $N(\text{H}_2)$ at 1200 GHz is given by (Lewis et al. 2022)

$$\kappa_{1200} = \frac{1}{f_{\text{mol}}\mu_{\text{H}_2}m_{\text{p}}\beta_{\text{K}}\gamma_{1200}} \quad (4)$$

where $\gamma_{1200} = A_{\text{K}}/\tau_{1200}$ and f_{mol} is the molecular gas fraction. We extracted a K-band extinction map from the iNICEST online

³ <https://www.cosmos.esa.int/web/herschel/ao2-documentation>

⁴ *Planck* Legacy Archive: <https://www.cosmos.esa.int/web/planck/pla>.

¹ <https://trao.kasi.re.kr/main.php>

² <https://www.iram.fr/IRAMFR/GILDAS>

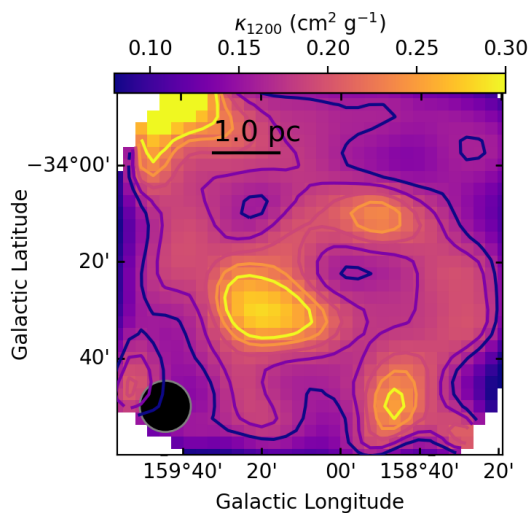


Fig. 2. Spatial variation in the 250 μm dust opacity in MBM12, κ_{1200} , derived from the ratio of τ_{1200} and A_K , accounting for variable molecular gas fraction. The conversion assumes an extinction curve with $R_V = 3.1$, and $N(\text{H})/A_K = 1.67 \times 10^{22} \text{ cm}^{-2} \text{ mag}^{-1}$ (Cardelli et al. 1989; Bohlin et al. 1978; Lewis et al. 2022). Contours of $\kappa_{1200} = [0.16, 0.18, 0.2, 0.22, 0.24] \text{ cm}^2 \text{ g}^{-1}$ are overplotted.

platform (Lombardi & Alves 2001; Lombardi 2009)⁵. We chose a control field close to MBM12, and a smoothing FWHM of $5'$, and a pixel size of $2.5'$. We then convolved and reprojected the τ_{1200} map to the same grid and used Eq. 4 to produce the spatial variation in κ_{1200} (Fig. 2). We also took spatial variations in f_{mol} into account (App. C). This $N(\text{H}_2)$ is then the molecular content, rather than the total hydrogen content along the line of sight. We are only considering the molecular cloud MBM12, as CO emission is emitted from inside a molecular cloud.

3.2. LTE CO column density

The method used to derive CO column densities for MBM12 is given in Montillaud et al. (in prep). We give a brief overview of the methodology here. We derived the CO column densities, $N(\text{CO})$, with large-scale TRAO CO line observations. We followed Pineda et al. (2010) to estimate $N(^{13}\text{CO})$. The main steps of the LTE estimate were estimating a T_{ex} map from the peak T_{mb} of each pixel's spectrum in the ^{12}CO map, assuming the same T_{ex} between ^{12}CO and ^{13}CO (Eq. 19 of Pineda et al. 2010). After the T_{ex} estimate, the ^{13}CO optical depth $\tau^{13}(\nu)$ was calculated for each channel width T_{mb} and the T_{ex} (Eq. 20 of Pineda et al. 2010). Lastly, ^{13}CO column density was calculated from $\tau^{13}(\nu)$ and T_{ex} (Eq. 17 of Pineda et al. 2010). Then $N(^{13}\text{CO})$ was converted to $N(\text{CO})$ by using the empirical isotopologue ratio with Eq. 4 of Szűcs et al. (2014), with the coefficients of model e in Table 3 of that paper. The different models consist of different initial conditions in their simulations. The choice of the model for the isotope ratio has around 20% systematic uncertainty, but it is much smaller than the uncertainty from assuming a constant isotope ratio (Szűcs et al. 2014). The assumption of the same excitation temperature between ^{12}CO and ^{13}CO adds uncertainty to our estimates (Padoan et al. 2000). To improve this estimate, one could either model the conversion of T_{ex} between two isotopologues, or one could survey the cloud in the ^{13}CO ($J = 2 - 1$)

⁵ <http://interstellarclouds.fisica.unimi.it/html/index.html>

line. However, modelling the difference of T_{ex} between the two isotopologues is non-trivial, and we did not have access to the ^{13}CO ($J = 2 - 1$) line at $2.5^\circ \times 3^\circ$ scales.

3.3. Virial analysis with CO

3.3.1. Dendrogram generation

We applied the dendrogram algorithm (Rosolowsky et al. 2008) with the `astrodendro` package to both CO spectral cubes. The algorithm assigns each voxel in the position-position-velocity (PPV) cube to one or more structures of connected isocontours. The structures are nested, with higher T_{mb} structures in PPV space always within lower T_{mb} structures. The trunk contains all the structures, while branches are structures with more structures within them. Structures that contain no further hierarchical structures are leaves. The minimum antenna temperature for a voxel to be considered for a structure is T_{min} . The minimum number of voxels for a structure is determined by the parameter N_{min} . The final parameter, ΔT_{min} , is the minimum T_{mb} difference between two peaks in PPV which could be considered as separate structures. We took $N_{\text{min}} = 27$, $T_{\text{min}} = 3\sigma_{\text{rms}}$, and $\Delta T_{\text{min}} = 3\sigma_{\text{rms}}$, following the suggestion of Rosolowsky et al. (2008).

3.3.2. Virial parameter estimates

We estimated the virial parameter α_{vir} for dendrogram structures assuming each structure corresponds to a sphere with mass M_{st} and radius R_{st} . We assume optically thin ^{13}CO emission, corresponding to a direct conversion factor between the sum of T_{mb} of the structure and the mass M_{st} (Eq. 5). The virial parameter α_{vir} was calculated for structures at all levels with Eq. 1. We used a locally calibrated $\langle X(^{13}\text{CO}) \rangle = 7.83 \times 10^{20} \text{ cm}^{-2} (\text{K km s}^{-1})^{-1}$ to convert T_{mb} to $N(\text{H}_2)$ (estimated in Sect. 4.1 and Fig. 5f). The benefit of using line observations with an empirical conversion from T_{mb} to $N(\text{H})$ to estimate α_{vir} is that velocity components can be considered individually, under the assumption that each velocity component corresponds to a respective gas clump. Separating structures into a dendrogram avoids spurious increases in $\sigma_{\text{v, st}}$ due to multiple velocity components along the line of sight. The mass estimate from the spectral cube was calculated as (Ladjele et al. 2020)

$$M_{\text{st}} = \delta A_{\text{pixel}} \mu_{\text{H}_2} m_{\text{H}} \langle X(\text{CO}) \rangle \times \sum_{\text{pixels}} \sum_{\text{channels}} \Delta v T_{\text{mb}}, \quad (5)$$

with δA_{pixel} the area of a single pixel, m_{H} the mass of a hydrogen atom and $\Delta v = 0.2 \text{ km s}^{-1}$ the channel width. The mass of larger hierarchical structure includes the mass of that structure's smaller scales. The pixel area $\delta A_{\text{pixel}} = s_{\text{pixel}, l} s_{\text{pixel}, b} d^2$ with s_{pixel} referring to the pixel scale and d the distance to MBM12. The radius R_{st} was estimated as

$$R_{\text{st}} = \left(\frac{A}{\pi} \right)^{0.5}, \quad (6)$$

with $A = \sum_{\text{pixels}} \delta A_{\text{pixel}}$ the total pixel area. The velocity dispersion per pixel $\sigma_{\text{v, pixel}}$ was calculated with

$$\sigma_{\text{v, pixel}} = \sqrt{\frac{\sum_{\text{channels}} T_{\text{mb}, i} (v_i - \bar{v})^2}{\sum_{\text{channels}} T_{\text{mb}, i}}}, \quad (7)$$

with T_i the antenna temperature in K, v_i the velocity of a channel i , \bar{v} the intensity-weighted mean velocity for the structure.

The velocity dispersion $\sigma_{v, \text{st}}$ was then the unweighted average of $\sigma_{v, \text{pixel}}$ for all sky pixels. The largest systematic uncertainties in our estimate of α_{vir} are spatial variation in $X(\text{CO})$, structure morphology, and distance. The $\langle X(\text{CO}) \rangle$ we use is the mean for MBM12; for low-density regions the true $X(\text{CO})$ can be significantly higher. The use of a constant $X(\text{CO})$ may underestimate the mass in low-density regions. Compared to the flux-weighted size from Rosolowsky et al. (2008), our estimate gives larger α_{vir} as we use the total area for the radius. These considerations suggest that our estimates of α_{vir} are upper limits (while α_{vir} further neglects external pressure and magnetic fields, Ballesteros-Paredes 2006). However, we point out that our use of a calibrated $X(\text{CO})$ from κ_v -calibrated $N(\text{H}_2)$ reduces the uncertainty on the observed value of α_{vir} significantly compared to assuming a $X(\text{CO})$ value from the literature. The distance we adopt has an uncertainty of 10%, which is systematic across the cloud, and so the uncertainty from distance is likely smaller than that from $X(\text{CO})$ and morphology.

3.4. Histogram of relative orientations

We applied FilDReaMS (Filament Detection and Reconstruction at Multiple Scales; Carrière et al. 2022a) to the *Herschel* dust column density maps of MBM12 described in Sect. 3.1. FilDReaMS is designed to detect elongated structures, which we will call filaments hereafter, in an image, and provides information on their widths, their orientations and the robustness of the detection. FilDReaMS uses a model template that has the shape of a rectangular bar (referred to as the model bar) defined by its length L_b , width W_b and aspect ratio $r_b = L_b/W_b$. We adopt $r_b = 3$ (Panopoulou et al. 2014; Arzoumanian et al. 2019; Carrière et al. 2022b), and we consider values of W_b spanning the range $[(W_b)_{\text{min}}, (W_b)_{\text{max}}]$, with $(W_b)_{\text{min}} = 5$ pix and $(W_b)_{\text{max}} = 29$ pix equal to the broadest structure detected in the map. The orientation angle of the model bar, ψ_b , is defined in the range $[-90^\circ, +90^\circ]$ and follows the IAU convention (Sect. A). For each value of W_b , FilDReaMS filters out structures broader than W_b and converts the resulting image into a binary map. At each pixel i of the binary map, FilDReaMS retrieves the orientation angle of the model bar that best matches the map, $(\psi_b)_i$, and computes the corresponding significance, S_i , which compares the detected filament to an ideal case (see Carrière et al. 2022a for more details). If $S_i > 1$, FilDReaMS confirms the detection of a filament with orientation angle $(\psi_f)_i = (\psi_b)_i$. Once all the pixels have been treated, FilDReaMS creates a filament mask by multiplying the above binary map with a model bar mask formed by the model bars of all the detected filaments. This filament mask is then applied to the initial image to reconstruct the physical network of detected filaments of bar width W_b with their true shapes. In case a given pixel belongs to two or more filaments, the filament orientation angle assigned to that pixel is the orientation angle of the most significant filament detected. This process is repeated over the entire range of W_b , leading to filamentary networks of different size scales.

4. Results

We identified four main regions separated by velocities in MBM12: The Horseshoe, Bow, North Compact and North Diffuse (Figs. 4 and 10). Figure 3 shows the mean spectra of the field. These maps were generated with emission $T_{\text{mb}} > 5\sigma_{\text{rms}}$. The Horseshoe is an isolated region around -6 km s $^{-1}$. The Bow and North Compact are connected in emission in ^{12}CO but not

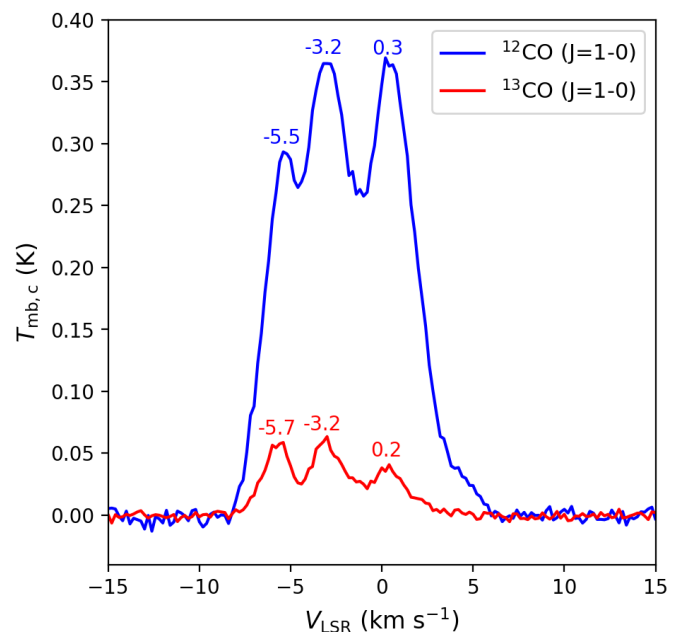


Fig. 3. Mean spectra over the entire MBM12 field. The velocities of each peak are indicated.

in ^{13}CO at around -2 km s $^{-1}$. North Diffuse consists of clumpy emission at > 1 km s $^{-1}$.

4.1. Environmental variation

For MBM12, we show the relations between $N(\text{H}_2)$, $N(\text{CO})$, $X(\text{CO})$ and $[\text{CO}/\text{H}_2]$, and their spatial distributions and PDFs. Figure 5 shows a comparison of most of these quantities to each other. Figs. 6 – 9 show their spatial distributions and PDFs.

The dust-opacity-calibrated $N(\text{H}_2)$ maps of MBM12 range from $N(\text{H}_2) = 2 \times 10^{20}$ cm $^{-2}$ to 1.3×10^{22} cm $^{-2}$. We generated a $N(\text{H}_2)$ probability density function (PDF) (Fig. 6). The PDF shows multiple bumps, which may be the result of the superposition of several independent column density distributions in the field.

We calculate $X(^{12}\text{CO})$ and $X(^{13}\text{CO})$ for the southern half of MBM12, by reprojecting the $40''$ *Herschel* $N(\text{H}_2)$ map to the TRAO CO integrated intensity maps at $44''$ resolution (Fig. 7). The morphology of $X(\text{CO})$ differs between the two isotopologues. In ^{12}CO , the distribution is continuous, while in ^{13}CO the Horseshoe is spatially disconnected from the Bow. The PDFs of $X(^{12}\text{CO})$ and $X(^{13}\text{CO})$ in Fig. 7c show double-peaked distributions connected by a powerlaw. We decompose the $X(\text{CO})$ PDFs into a lognormal at the peak with a truncated power law. The fitting equations and results of the fit are given in App. E. The combination of these distributions well described the $X(\text{CO})$ PDFs, except an excess at $X(^{12}\text{CO}) = 10 X_{\text{Gal}}$ and $X(^{13}\text{CO}) = 40 X_{\text{Gal}}$. Lognormal PDFs with deviations for $X(\text{CO})$ have been seen in $8.6'$ resolution maps by (Lewis et al. 2022, App. B). We consider physical explanations for the $X(\text{CO})$ PDF in Sect. 5.2.

The $N(\text{CO})$ varies in MBM12 from 1×10^{16} cm $^{-2}$ up to 1×10^{18} cm $^{-2}$ (Fig. 8). The distribution of $N(\text{CO})$ shows filamentary structure in the Horseshoe. In North Compact, there are some peaks, but $N(\text{CO})$ is relatively constant throughout the structure. The abundances $[\text{CO}/\text{H}_2]$ in MBM12 have an average of 5.9×10^{-5} . The spatial distributions of the $[\text{CO}/\text{H}_2]$ have some interesting variation. At the centre of the Horseshoe, the abundances are between $4 \times 10^{-5} - 1 \times 10^{-4}$, with a clumpy spa-

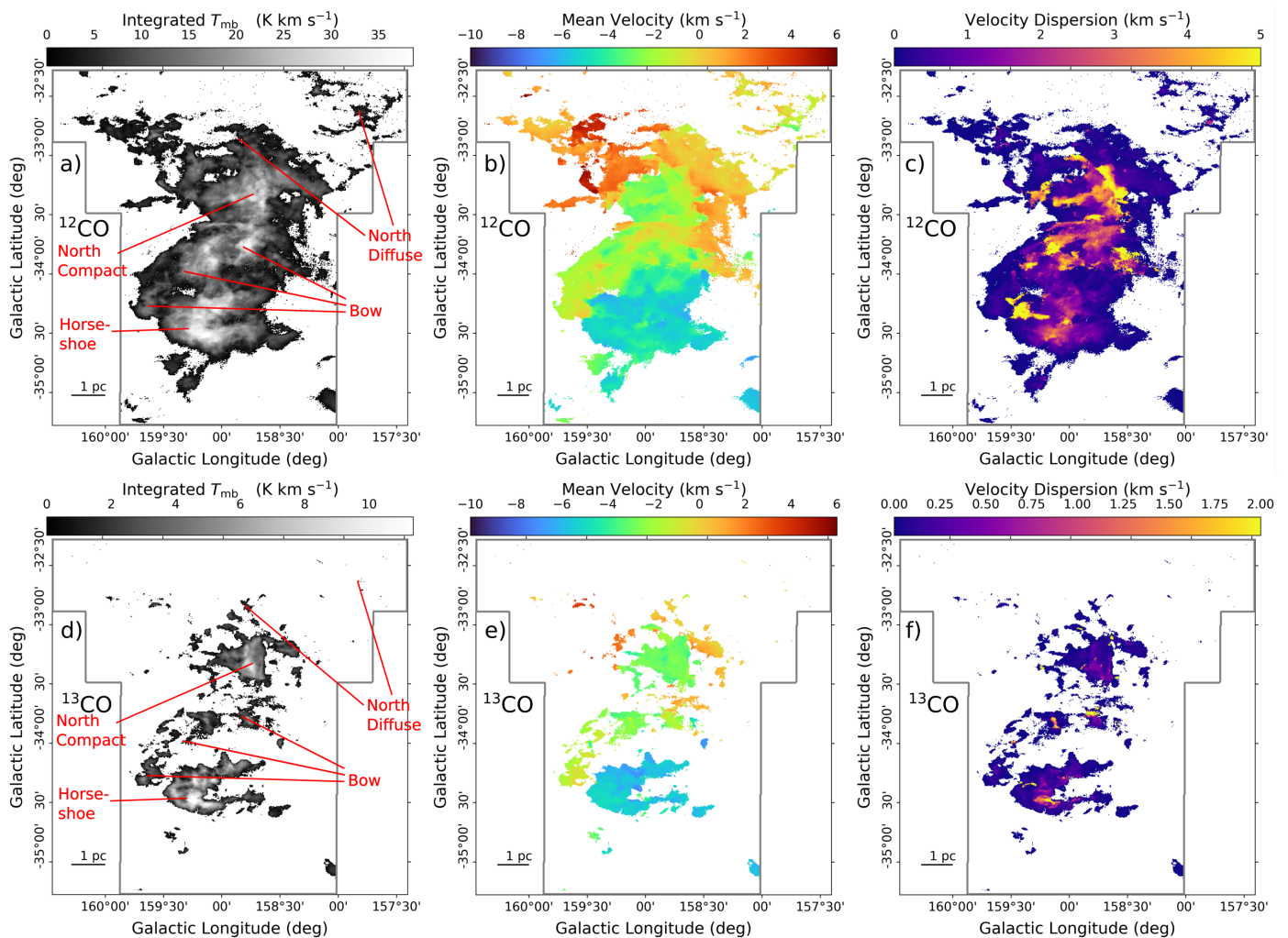


Fig. 4. Integrated intensity (a and d), intensity weighted mean velocity (b and e) and intensity weighted velocity dispersion (c and f) for ^{12}CO (top) and ^{13}CO (bottom) for MBM12 as observed with the TRAO. The sub-regions of MBM12 referenced in the text are labeled in red.

tial distribution. The northern islands in the Bow show centrally peaked $[\text{CO}/\text{H}_2]$ (Fig. 9). The abundances are lognormal, centred at the average abundance. The abundance shows a power-law tail at the lower end.

We compare our multi-tracer observables in Fig. 5. Three main features are: (i) the quasi-linear dependence of $N(\text{CO})$ with $N(\text{H}_2)$ (panel d) leading to an average uniform CO abundance $[\text{CO}/\text{H}_2]=5.9\times 10^{-5}$, (ii) at low $N(\text{H}_2)$ (panel e), the two large excursions of $W(^{12}\text{CO})$ below and above the average quasi-linear increase of $W(^{12}\text{CO})$ with $N(\text{H}_2)$, corresponding to $\langle X(^{12}\text{CO}) \rangle = X_{\text{Gal}}$. These one-dex excursions are responsible for the shape of the $X(^{12}\text{CO})$ distribution with $N(\text{H}_2)$ (panel j): the former, at the origin of the rise of $X(^{12}\text{CO})$ above X_{Gal} at $N(\text{H}_2)$ below $1.5 \times 10^{21} \text{ cm}^{-2}$, is due to the drop of the CO abundance in the least UV-shielded layers while the latter, at the origin of all the $X(^{12}\text{CO})$ values below X_{Gal} , traces the fall-off of collisional de-excitation in low density gas, and (iii) the quasi-linear increase of $W(^{13}\text{CO})$ with $N(\text{H}_2)$ (panel f) leading to a ^{13}CO integrated intensity close to 4 times weaker than that of ^{12}CO , a result in agreement with early galactic CO and ^{13}CO line surveys that found that ^{12}CO lines are ~ 5 times brighter than ^{13}CO lines (Stark et al. 1983).

4.2. Multi-scale dynamics

4.2.1. How to interpret dendrograms

The dendrogram algorithm is a useful way of segmenting PPV cubes into hierarchical structures. Our use of dendrograms assumes each voxel in PPV corresponds to a mass proportional to the voxel's T_{mb} (Rosolowsky et al. 2008). From Eq. 1 and the dendrogram algorithm, some considerations can be drawn. Higher in the hierarchy, the structures become smaller and have a higher average T_{mb} . Therefore, one would generally expect α_{vir} to decrease as one moves up the dendrogram hierarchy. A similar pattern should be expected for velocity dispersion. Therefore, looking only at the leaves of a dendrogram will systematically underestimate α_{vir} , as one ignores the pressure, shear and gravitational effects of the larger parent structure on α_{vir} (Ballesteros-Paredes 2006). Therefore, it is helpful to look at the full hierarchy of α_{vir} estimates. Virial parameters are calculated per structure, and are therefore difficult to visualize spatially. We produced a plot where we layer the contours of the structures, starting from the lowest hierarchical structure (i.e. the largest structure spatially). The contour is coloured by the value of the respective variable, either V_{LSR} or α_{vir} . We then successively layer the sub-structures on top of the largest structures to produce a two-dimensional visualization. This works well for sim-

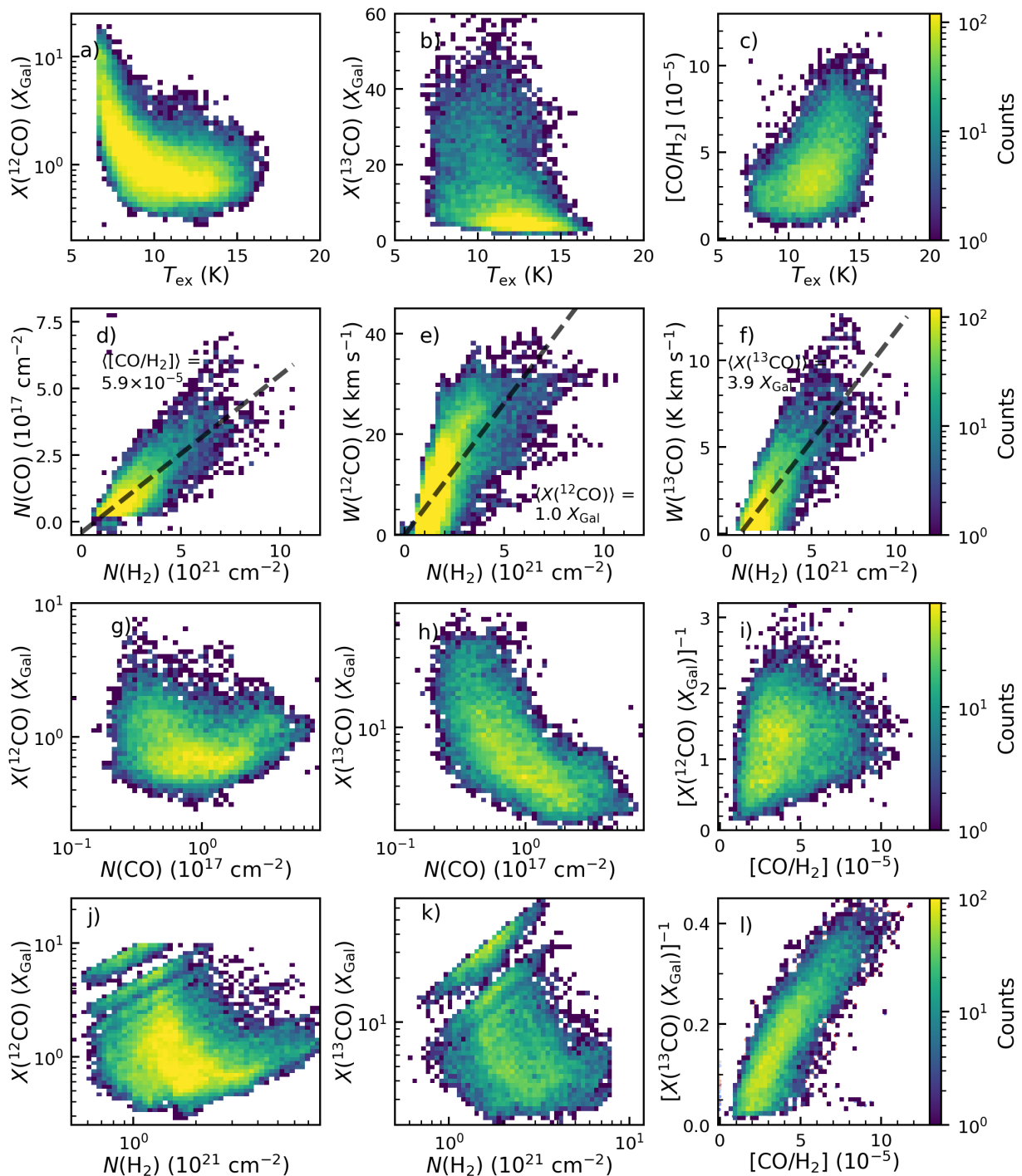


Fig. 5. Comparison of H_2 and CO quantities observed in MBM12 with Herschel and TRAO. We compare $N(\text{H}_2)$ with CO linewidths $W(\text{CO})$, X-factors $X(\text{CO})$, ^{12}CO excitation temperature T_{ex} , CO column density $N(\text{CO})_{\text{lte}}$ and CO abundances $[\text{CO}/\text{H}_2]_{\text{lte}}$. Panels a)–c) and d)–l) have different colorscales. Panels d)–f) have linear fits shown in black lines, with the slope annotated on the respective panel. The linear striations at low $N(\text{H}_2)$ in panels j) and k) are artefacts of the sigma-clipping in the $W(\text{CO})$ estimates.

pler dendrograms, such as ^{13}CO in MBM12 (Fig. 10). We colour the dendrogram tree diagrams with V_{LSR} and α_{vir} , and annotated the respective sub-structures (panels c and d of Figs 10). Virial parameters alone are not conclusive indicators of gravitational collapse, as they measure energy balance rather than stability. (Ballesteros-Paredes 2006; Offner et al. 2022; Chevance et al. 2023).

4.2.2. Hierarchical structure in MBM12

The ^{13}CO emission is separated into the North-Diffuse, Bow, North-Compact and Horseshoe subregions (Fig. 10).

The North Diffuse subregion has a ring shape in the north of MBM12, with most structures having $\alpha_{\text{vir}} > 4$ (also seen in Pound et al. 1990). The North Diffuse region has the same velocity as the small northern clumps at $V_{\text{LSR}} \sim 4 \text{ km s}^{-1}$.

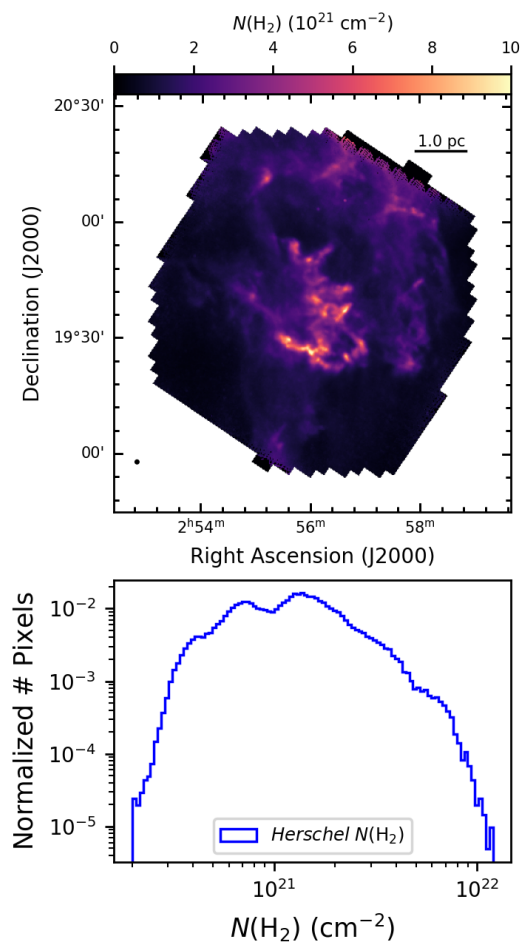


Fig. 6. Top: Opacity-calibrated $N(\text{H}_2)$ map from *Herschel* observations. Bottom: Dust-opacity-calibrated $N(\text{H}_2)$ PDF with *Herschel* for MBM12. The *Herschel* map covers only the southern half of MBM12.

The Bow subregion has two components in ^{13}CO , east at $V_{\text{LSR}} \sim -1 \text{ km s}^{-1}$ and west at -2.5 km s^{-1} . This subregion is also detected with *Herschel*. The eastern Bow at -1 km s^{-1} is likely denser than the western Bow, with $\alpha_{\text{vir}} \lesssim 2.5$, and thin layers of large $X(^{13}\text{CO})$ (middle panel of Fig. 7). The western Bow has two islands, the most western island with $\alpha_{\text{vir}} > 5$, and an eastern island with $\alpha_{\text{vir}} \sim 2$. The western Bow has thicker layers of large $X(^{13}\text{CO})$ (middle panel of Fig. 7) than the eastern Bow.

The North Compact subregion has complex hierarchical structure. It was not covered with *Herschel*. It has some sub-structures with $\alpha_{\text{vir}} > 5$ (panel d of Fig. 10), but the whole structure has $\alpha_{\text{vir}} \sim 3$. The region has the largest $N(\text{CO})$ in the north of MBM12 (Fig. 8) but is not strongly centrally peaked. There are single structures in this subregion (Fig. 11) with $\alpha_{\text{vir}} < 2$, but most of this structure has $\alpha_{\text{vir}} > 2$.

The Horseshoe, at $V_{\text{LSR}} = -5.5 \text{ km s}^{-1}$ has the most complex hierarchical structure in MBM12. Some structures at the southern part of the Horseshoe have $\alpha_{\text{vir}} > 5$ (Fig. 10 b). Some of these may be fore- or background clumps, as they are also at different velocities. The Horseshoe has the largest average $N(\text{H}_2)$ in MBM12 and has $\alpha_{\text{vir}} \sim 3$.

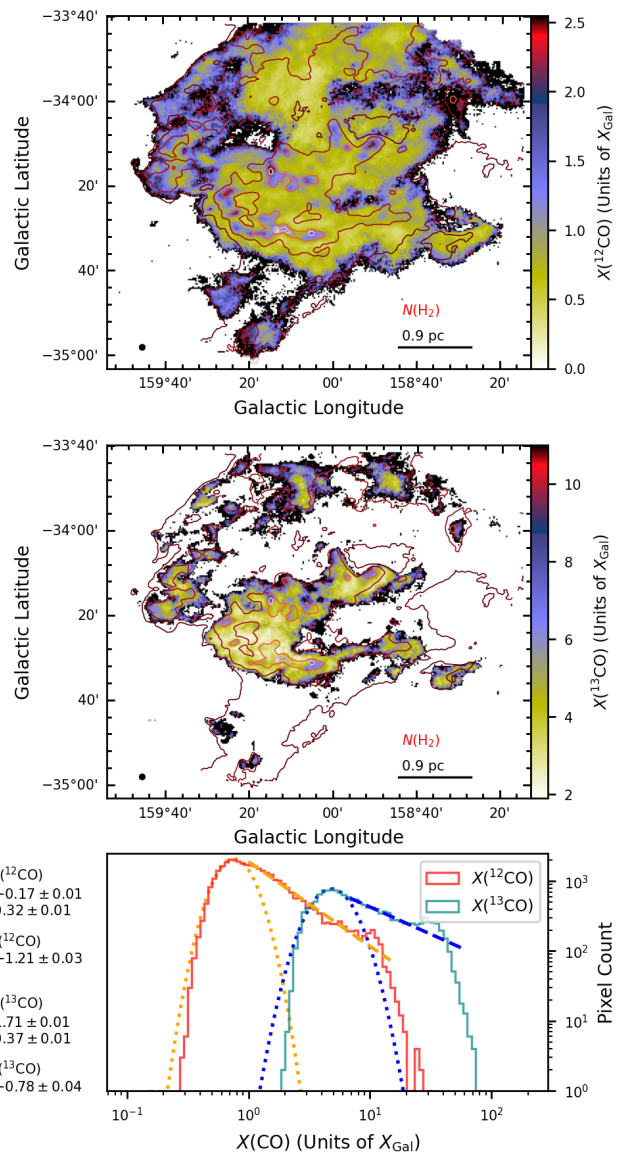


Fig. 7. Ratio of $N(\text{H}_2)$ and CO line area for ^{12}CO and ^{13}CO ground state rotational transitions in the southern half of MBM12. The figures are in units of $X_{\text{Gal}} = 2 \times 10^{20} \text{ cm}^{-2} (\text{K km s}^{-1})^{-1}$. The beam size and linear scale are shown at the bottom left and right respectively. Contours of $N(\text{H}_2)$ are shown in red at levels of $[1, 2, 5, 8, 10] \times 10^{21} \text{ cm}^{-2}$. The bottom panel shows the PDFs of $X(^{12}\text{CO})$ and $X(^{13}\text{CO})$.

4.2.3. Scale dependence of α_{vir}

We examine the interdependence of M_{st} and α_{vir} on R_{st} for the largest structures identified in the ^{13}CO dendrogram (Fig. 10c). We fitted a broken power law to the masses M_{st} and radii R_{st} of ^{13}CO dendrogram structures in MBM12. The functional form is

$$\left(\frac{M_{\text{st}}}{1M_{\odot}}\right) = A_i \left(\frac{R_{\text{st}}}{1\text{pc}}\right)^{\alpha_i} \quad (8)$$

where $i = 1$ if $R_{\text{st}} < R_{\text{break}}$ and $i = 2$ if $R_{\text{st}} > R_{\text{break}}$. The best fit parameters with uncertainties are shown in Tab. 1. To ensure continuity between the two power laws, from Eq. 8 the break-point R_{break} can be calculated directly:

$$R_{\text{break}} = \left(\frac{A_1}{A_2}\right)^{\frac{1}{\alpha_2 - \alpha_1}} \quad (9)$$

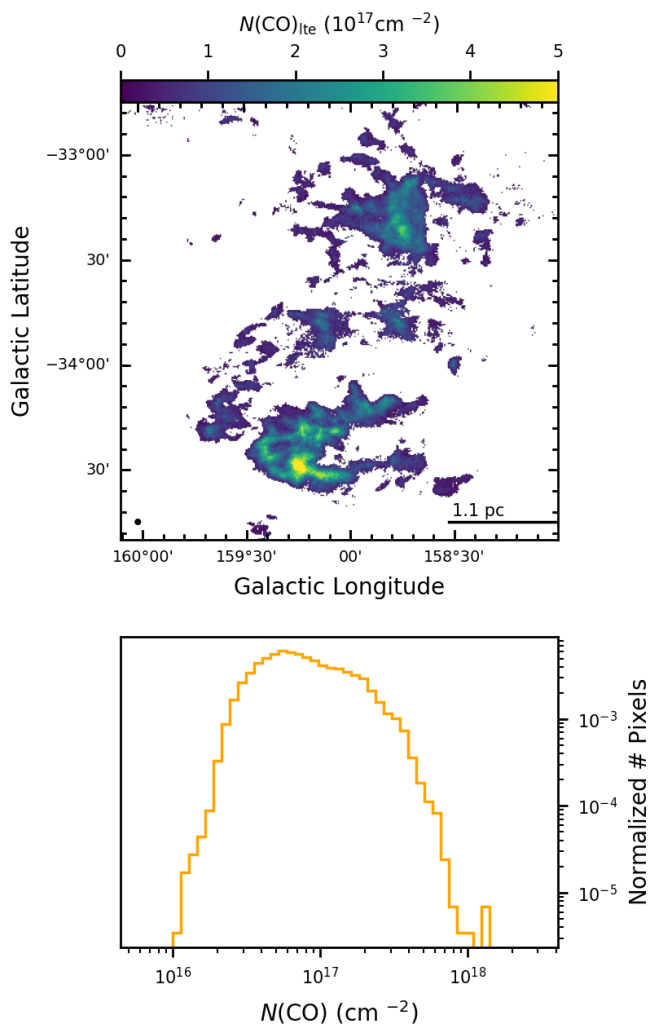


Fig. 8. Carbon monoxide column density $N(\text{CO})$ for MBM12, derived from TRAO ^{12}CO and ^{13}CO ($J = 1-0$) observations. The map shown on the top was estimated with standard LTE assumptions to derive $N(^{13}\text{CO})$ and converted to total $N(\text{CO})$ with isotopologue ratio function from Szűcs et al. (2014). The bottom panel shows the PDF for the $N(\text{CO})$ map.

From the dendrogram we take trunk-level structures that have more than eleven sub-structures. Spatial investigation reveals that these structures are the horseshoe, North Compact, eastern Bow, western Bow, southern North Diffuse, and eastern North Diffuse. We then plot the mass-size relation normalized by R_{st}^2 , and the surface density dependence of α_{vir} for all hierarchical structures (Fig. 11). Note that these data points are not independent, as they share voxels in PPV. Therefore we are rather estimating the slope of the change in mass with radius, comparable to the differential virial analysis of (Krumholz et al. 2025). We found correlations between mass and radius, that are best described by a broken power laws (Fig. 11 a). Tab. 1 show the scaling parameters A_i , power law slopes α_i and break points R_{break} for all the substructures. The large scale ($R_{\text{st}} > R_{\text{break}}$) indices were close to $M \propto R^2$ for the Horseshoe and eastern Bow with $\alpha_2 = 1.91 \pm 0.02$ and $\alpha = 1.92 \pm 0.03$ respectively. For the other subregions, the outer power law index is sub-Larson, with $\alpha_2 < 1.5$. The outer scaling factor A_2 varies between 54 – 169, with the largest value at the Horseshoe, and the smallest at North Diffuse subregions. However, the power law

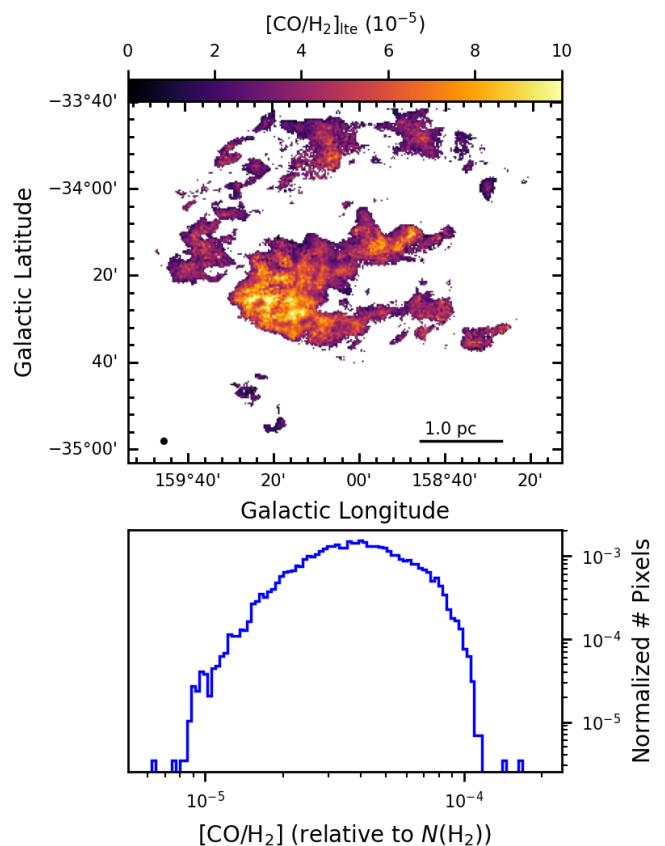


Fig. 9. Map of CO abundance relative to H_2 column densities in the southern part of MBM12. The top panel shows $N(\text{CO})$ estimated from LTE assumptions. The bottom panel shows the abundance PDF.

index is super-Larson for all low-mass subregions in the inner power law, with $\alpha_1 > 2$, and the statistically significant scaling factors A_1 varying between 50–215. The virial parameter is increasing with decreasing Σ_{st} . The North Compact is the only region which contained $\alpha_{\text{vir}} < 2$ structures. However, α_{vir} has some variation depending on the scale at which the structure is analysed. Many of the smallest scale structures in the Horseshoe and North Compact have large $\alpha_{\text{vir}} > 2$. The other structures have $\alpha_{\text{vir}} \sim 8$ at parsec scales (Fig. 11 b), with variability in α_{vir} towards smaller scales. No structures in eastern Bow, western Bow, southern North Diffuse, eastern North Diffuse have $\alpha_{\text{vir}} \sim 2$ at any scale.

4.3. Histograms of relative orientations

We examine the relative orientation between $N(\text{H}_2)$ structures and the plane-of-sky magnetic field \mathbf{B}_{PoS} . Figure 12 summarizes our histogram of relative orientation analysis in MBM12. The top left panel shows the *Herschel* $N(\text{H}_2)$ map, from which networks of filaments were extracted. These networks are shown in the top middle and top right panels, with the largest- W_b and smallest- W_b filaments per pixel shown. These figures reveal very thin and low- $N(\text{H}_2)$ striations around the Horseshoe and Bow subregions. The Horseshoe has significantly thicker filaments than the Bow, with bar widths ~ 0.6 pc, with a finer, continuous structure, while the Bow appears more disconnected, with bar widths of ~ 0.4 pc. The middle row of Fig. 12 shows maps of the relative orientation between filaments and \mathbf{B}_{PoS} for the smallest- W_b filaments (left panel), largest- W_b filaments (right panel), and

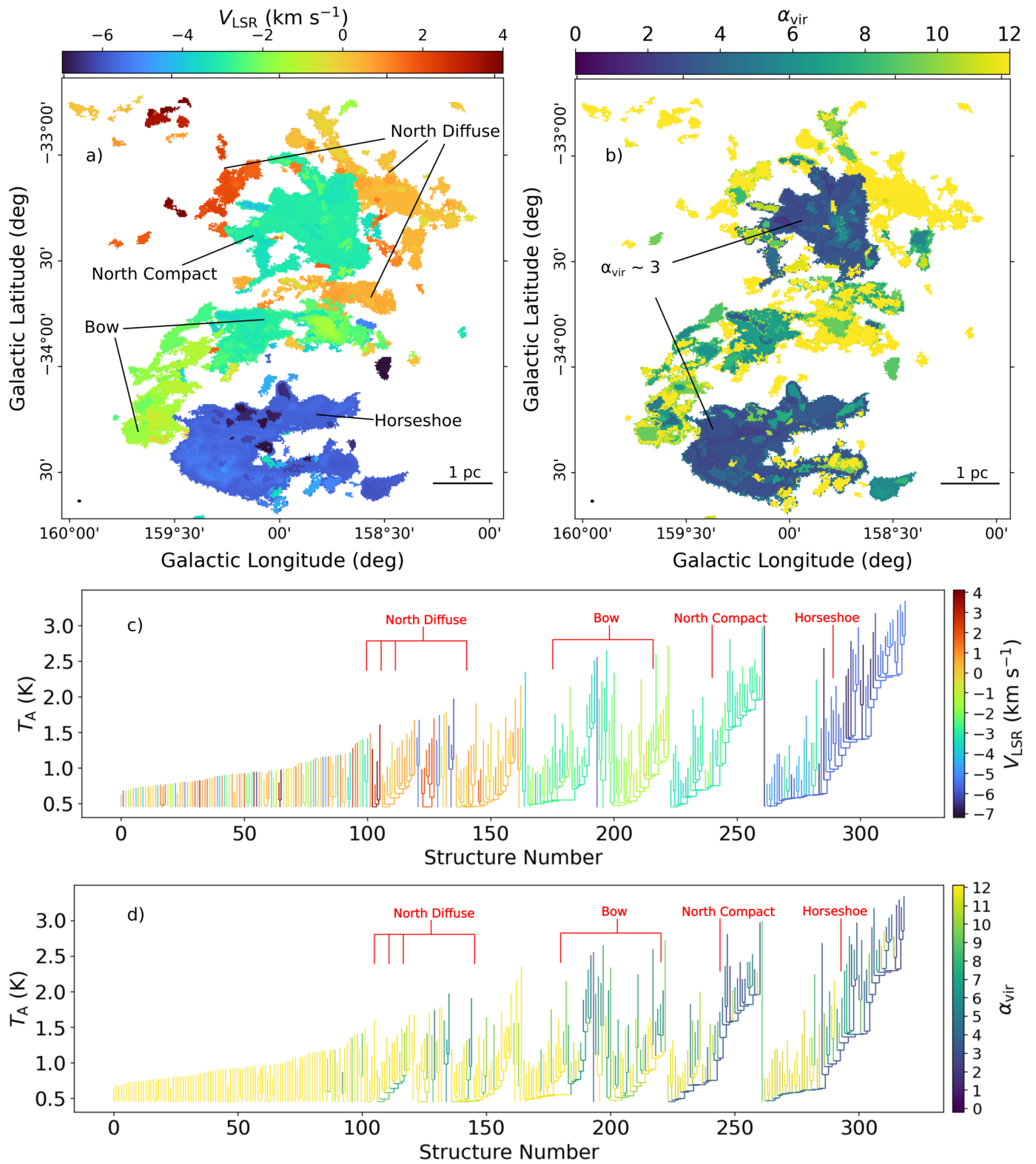


Fig. 10. Hierarchical structure and virial estimates for MBM12 with ^{13}CO ($J = 1 - 0$) observations with the TRAO. Panel a: Centre velocities for dendrogram structures. The plot is made by plotting the largest scale structures first with a single colour corresponding to their V_{cen} , and then the smaller scale structures are plotted on top. Panel b: Virial parameter estimates for dendrogram structures. The plot is made in the same way as panel a, but with the color defined by the value of α_{vir} . Panel c: Tree diagram for ^{13}CO observations of MBM12. The tree diagram is coloured according to the value of V_{cen} for the structure with the same colour scale as panel a. The four largest-scale structures are shown in red. Panel d: Tree diagram for α_{vir} estimated with the ^{13}CO observations of MBM12. The tree diagram is coloured according to α_{vir} with the same colour scale as panel b.

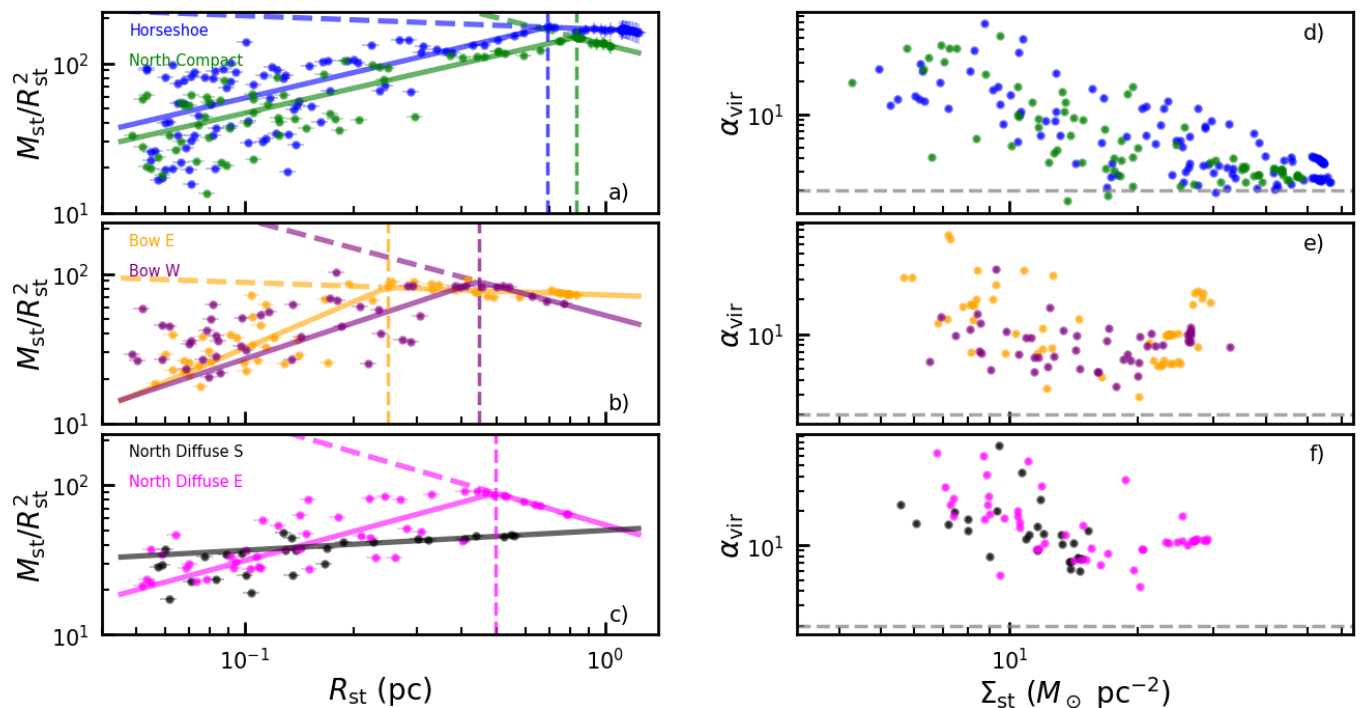


Fig. 11. Scale dependence of ^{13}CO dendrogram structures in MBM12. The colors are for the Horseshoe (blue), North Compact (green), eastern Bow (yellow), western Bow (purple), southern North Diffuse (black) and eastern North Diffuse (grey). Broken power law fits are also shown, with the respective fit values in Tab. 1. Vertical lines indicate the power law breaking point. The vertical axis of panels a) - c) ($M_{\text{st}}/R_{\text{st}}^2$) is in units of $M_{\odot} \text{pc}^{-2}$.

Table 1. Fitted parameters for the broken power law fits to the mass-size relations (Fig. 11).

ID	Subregion	A_1	α_1	A_2	α_2	R_{break} (pc)
1	Horseshoe	215 ± 8	2.56 ± 0.06	169 ± 1	1.91 ± 0.02	0.69
2	North Compact	165 ± 2	2.55 ± 0.03	134 ± 1	1.40 ± 0.04	0.83
3	Bow E	339 ± 312	3.02 ± 0.55	73 ± 1	1.92 ± 0.03	0.25
4	Bow W	170 ± 28	2.80 ± 0.16	53 ± 2	1.36 ± 0.07	0.45
5	North Diffuse S	50 ± 1	2.13 ± 0.02	–	–	–
6	North Diffuse E	139 ± 19	2.65 ± 0.16	54 ± 2	1.30 ± 0.09	0.50

Notes. The parameters (A_1, α_1) were for $R_{\text{st}} < R_{\text{break}}$, while (A_2, α_2) was for $R_{\text{st}} > R_{\text{break}}$. North Diffuse S is fit with a single power law.

most significant filaments across all W_b (center panel). The bottom row of Fig. 12 shows the histograms of relative orientations as a function of $N(\text{H}_2)$ for the same sets of filaments. At small scales, most filaments are roughly parallel to \mathbf{B}_{PoS} at low $N(\text{H}_2)$, with $|\psi_f - \psi_B| \lesssim 35^\circ$ for $N_{\text{H}_2} \leq 4.5 \times 10^{21} \text{cm}^{-2}$, while high- $N(\text{H}_2)$ filaments have more random orientations, with a small preference towards -45° . The situation is clearer for the most significant and largest- W_b filaments. Similarly, most filaments at low- $N(\text{H}_2)$ are roughly parallel to \mathbf{B}_{PoS} while the high- $N(\text{H}_2)$ filaments, which correspond to the Horseshoe, shows that the northern part is mostly parallel to \mathbf{B}_{PoS} and the southern part is roughly perpendicular to \mathbf{B}_{PoS} . The HROs in MBM12 seem to indicate that at low- $N(\text{H}_2)$ filaments tend to be smaller and oriented parallel to the magnetic field. As the $N(\text{H}_2)$ increases, the filament size also increases, and these large scale filaments are either parallel or perpendicular to the magnetic field. At high $N(\text{H}_2)$, structures are located in the southern part of the Horseshoe, perpendicular to the magnetic field, where both the large scale filaments are co-spatial in the plane of the sky.

5. Discussion

5.1. Dust opacity variation and $N(\text{H}_2)$ estimation

The dust opacity κ_v is a function of various dust properties (size distribution, chemical composition and structure). Dust models can predict κ_v among other things (e.g. Hensley & Draine 2023; Ysard et al. 2024). It is known that the far-infrared dust opacity varies in the diffuse ISM, with less pronounced variations in NIR extinction (Planck Collaboration et al. 2014b; Reach et al. 2015; Nguyen et al. 2018). Between the diffuse ISM and molecular clouds, there is a factor of three change in the ratio of the $250 \mu\text{m}$ and NIR opacities (Juvella et al. 2015). Empirical κ_v calibration is important as column density estimates propagate into mass, density and abundance estimates. We summarise some methods for estimating κ_{1200} in Table 2 (see App. D). We recommend the κ_v calibration method of Lewis et al. (2022) with NIR extinction. Even if NIR extinction maps do not have high resolution, they can give a cloud averaged κ_v , or spatial variation in some cases that is better than assuming a constant from literature. The NIR extinction to column density ratio is not necessarily con-

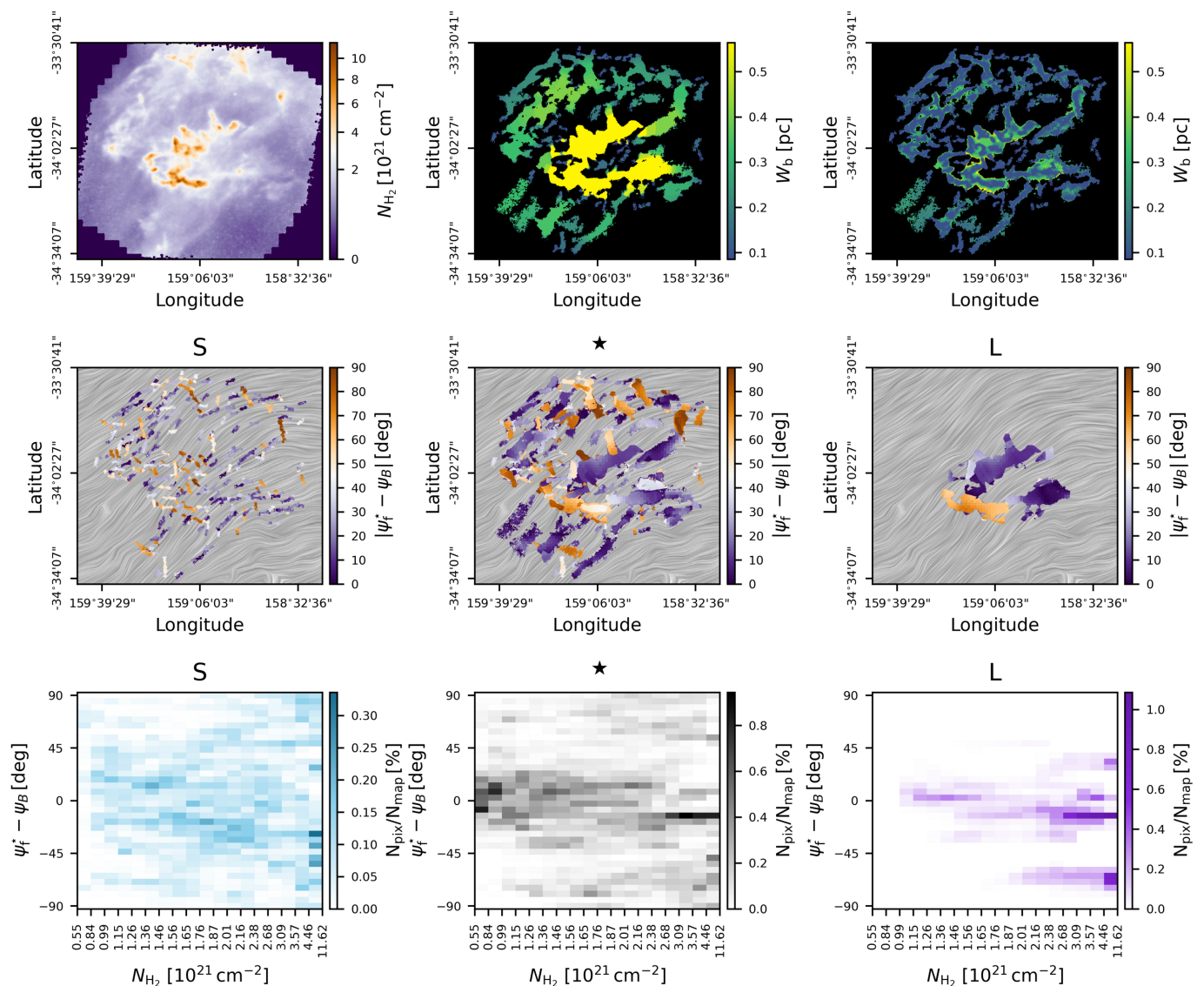


Fig. 12. Top left: MBM12 H₂ column density map. Top middle: Network of filaments reconstructed with FilDReaMS, with the largest bar width, W_b , per pixel shown. Top right: Same network of filaments with the smallest W_b per pixel shown. Middle left, middle and right: Map of the relative orientation for the smallest W_b filaments, most significant filaments across W_b and largest W_b filaments respectively. \mathbf{B}_{PoS} orientation is visualised using line integral convolution (LIC) in grayscale in the background. Bottom left, medium and right: Histograms of relative orientations as a function of $N(\text{H}_2)$ for the smallest W_b filaments, most significant filaments across W_b and largest W_b filaments respectively.

stant if R_V varies, but the empirical models of Hensley & Draine (2023) can be used to quantify the uncertainty of R_V . Informed use of κ_V would remove bias in masses and chemical abundances in diverse star forming environments.

5.2. Intra-cloud $X(\text{CO})$ variations

The $X(\text{CO})$ factor is a measure of H₂ molecules per CO emission. On theoretical grounds we expect it to be affected by CO abundances, H₂ kinetic temperature, H₂ density, dust temperature and the surrounding radiation field (Shetty et al. 2011; Lewis et al. 2021). Molecular H₂ and CO are photodissociated in the interstellar radiation field if shielding is too weak (van Dishoeck & Black 1988; Gong et al. 2018). Shielding can occur due to self-shielding, shielding by other molecules or attenuation by dust (van Dishoeck & Black 1988). Molecular hydrogen forms at low densities ($> 30 \text{ cm}^{-3}$) with efficient

self shielding, while CO requires dust to attenuate the radiation and therefore forms at hydrogen densities $> 100 \text{ cm}^{-3}$ (van Dishoeck & Black 1988; Glover et al. 2010; Gong et al. 2018). In these intermediate densities $30 - 100 \text{ cm}^{-3}$ is CO dark gas, which would lead one to expect $X(\text{CO}) \rightarrow \infty$ as CO starts to form at the outer edges of molecular clouds. However observations of diffuse clouds have rather found $X(\text{CO}) \leq X_{\text{Gal}}$ (Liszt et al. 2010; Liszt & Pety 2012). This can be explained by low collisional de-excitation for CO at low densities, where CO is more effective per H₂ molecule at emission (Hennebelle & Falgarone 2012). The variance of the $X(\text{CO})$ factor is also very high in diffuse regions, where $n_{\text{H}_2} < 400 \text{ cm}^{-3}$ (Shetty et al. 2011). Deeper into the cloud, where A_V is between 1 and 2 mag, the dust shields the interstellar radiation field (ISRF) for the formation of CO, $X(\text{CO})$ exponentially decreases (Shetty et al. 2011; Szűcs et al. 2016). However, at the largest densities, the lines may self-absorb, or CO

Table 2. Summary of κ_{1200} estimating strategies and the consequent values.

No.	Method	κ_{1200} ($\beta = 2$) ($\text{g}^{-1} \text{cm}^2$)	Range in κ_{1200} ($\text{g}^{-1} \text{cm}^2$)	References
1	Common Literature	0.1	N/A	(Hildebrand 1983)
2	Common Literature	0.144	0.136 – 0.149 ^a	(Beckwith et al. 1990)
3	Survey	0.093 ± 0.016	0.065 – 0.12 ^b	(Lewis et al. 2022)
4	Survey	0.112±0.014	0.084 – 0.280	(Juvela et al. 2015)
5	Calibrator $N(\text{H})$	0.124±0.006	0.124 – 0.176 ^c	(Remy et al. 2017)
6	Calibrator $N(\text{H})$	0.192±0.007	0.16 – 0.24 ^d	Extinction with NICEST (Sect. 3.1)

Notes. For the determinations of the values and ranges, see App. D. ^(a) For $\beta = 1.7 - 2.2$. ^(b) For $\beta = 1.7 - 2.2$ between 353 GHz and 1200 GHz. ^(c) For $f_{\text{mol}} = 0.7 - 1$. ^(d) Spatial variation.

is frozen onto dust grains, which then increases $X(\text{CO})$ again (Pineda et al. 2010; Szűcs et al. 2016). We see these regimes in Fig. 5 j and k. For $N(\text{H}_2)$ below 10^{21} cm^{-2} , we have high $X(^{12}\text{CO})$ values, but also many where $X(^{12}\text{CO}) < X_{\text{Gal}}$. The mean value of $X(^{12}\text{CO})$ was very close to the galactic average recommended by Bolatto et al. (2013). Our estimate is twice the value of $\approx 0.5X_{\text{Gal}}$ surrounding MBM12 from Remy et al. (2017). In Perseus $X(^{12}\text{CO})$ was measured as $0.5 - 1.5X_{\text{Gal}}$ (Pineda et al. 2008). The relationship between $X(\text{CO})$ and $N(\text{H}_2)$ has been investigated theoretically and through observations of the California MC as well (Kong et al. 2015; Szűcs et al. 2016; Lewis et al. 2021). Magnani et al. (1988) calculated $X(\text{CO})$ for various high-latitude clouds (excluding MBM12) and found an average value of $X(\text{CO}) = 3.2 \pm 0.6 X_{\text{Gal}}$ for their full sample, or $1.6 X_{\text{Gal}}$ if they excluded some dark clouds. They also estimated abundances of $4 - 12 \times 10^{-5}$ which is closer to our estimate of MBM12 than to the average Milky Way value. Cotten & Magnani (2013) estimated $X(\text{CO}) = 0.65 X_{\text{Gal}}$ for MBM 40. In MBM16, $X(\text{CO}) = 3.6 X_{\text{Gal}}$ and in MBM40 $X(\text{CO}) = 1.3 X_{\text{Gal}}$ (Magnani et al. 1998). The $X(\text{CO})$ PDFs possibly encode this chemical behaviour (Fig. 7). Close to the average value of $X(\text{CO})$ the PDF was lognormal, with a similar standard deviation of around $1.4 X_{\text{Gal}}$. In App E, we use the statistical behaviour of the $X(\text{CO})$ PDF to visualize the physical transitions in MBM12 Fig. E.1. If other molecular clouds show similar lognormal and powerlaw behaviour in their $X(\text{CO})$ PDFs, the PDF properties can be used as a measure of chemistry and excitation. Most works only focus on $X(\text{CO})$ as a conversion factor for mass. However, our 44'' investigation of $X(\text{CO})$ implies that it may be a useful probe of molecular cloud substructure in its own right. Radiative transfer modelling of the $X(\text{CO})$ PDFs physical dependencies combined with estimates from more sources may reveal if $X(\text{CO})$ PDFs have any diagnostic potential.

5.3. CO abundances

The highest CO column densities in MBM12 was $1 \times 10^{18} \text{ cm}^{-2}$. The high column densities are associated with the Horseshoe and North Compact (Fig. 8). The measured $N(\text{CO})$ for MBM12 of a few 10^{17} is higher than any MBM clouds in the sample of van Dishoeck et al. (1991). The mean $[\text{CO}/\text{H}_2]$ of 5.91×10^{-5} of MBM12 is lower than the canonical 10^{-4} in Milky Way clouds such as Taurus and Orion B (Pineda et al. 2010; Bolatto et al. 2013; Roueff et al. 2021). Low abundances like this have been observed before (Burgh et al. 2007; Liu et al. 2013; Luo et al. 2023). The methodological assumptions that go into abundance calculations (κ_{ν} for $N(\text{H}_2)$, constant T_{ex} , isotope ratio, LTE only vs non-LTE) make precise comparison with other works difficult. In the case of Taurus Pineda et al. (2010), assumed a con-

stant isotope ratio of 69, which increases their $N(\text{CO})$ estimate by up to 70%, compared to our use of a variable isotope ratio (Szűcs et al. 2014). Variable isotope ratio would also change the shape of the $N(\text{CO})$ and $[\text{CO}/\text{H}_2]$ PDFs. The environmental differences between Taurus and MBM12 play a role in the abundance differences.

5.4. Virial analysis in MBM12

We used virial analysis as one tool among many for assessing virial equilibrium. In App. F we discuss some of the historical ambiguities in the interpretation of α_{vir} . We find $\alpha_{\text{vir}} \gtrsim 3$ for all regions in MBM12. In all cases, α_{vir} did not vary significantly with scale. The scale independence of α_{vir} has also been seen in other regions, including Serpens South and NGC 253 (Luo et al. 2024; Friesen & Jarvis 2024; Oakes et al. 2025). Scale independent α_{vir} is expected for structures. If the structures follow Larson’s laws, $M_{\text{st}} \propto R_{\text{st}}^2$ and $\sigma_{\text{v,st}} \propto R_{\text{st}}^{0.5}$, then from Eq. 1 $\alpha_{\text{vir}} \propto \sigma_{\text{st}}^2 R_{\text{st}} M_{\text{st}}^{-1} \propto 1$. The scaling factors in front of the mass-size relations (Fig. 11) in the Horseshoe are up to three times higher than that of the northern regions. The $M_{\text{st}} \propto R_{\text{st}}^2$ and $\sigma_{\text{v,st}} \propto R_{\text{st}}^{0.5}$ hierarchy is the locus of the gravitational instability threshold of self-gravitating polytropes of increasing temperature immersed in a common pressure reservoir P_{ext} . The structures of this hierarchy are the result of fragmentation of the larger scales, which occurs prior to collapse, and behave as a N-body system in virial equilibrium (Chieze 1987). The interesting point here is that the pre-factor of the mass-size relation is proportional to $P_{\text{ext}}^{0.5}$ which shows that the external pressure of the structures of lowest α_{vir} is about 10 times larger than that of the structures of largest α_{vir} . For a turbulent core with a constant surface density, an increased internal pressure (which is related to the external pressure) should increase α_{vir} (McKee & Holliman 1999; McKee & Tan 2003). We do observe that the smaller scale structures $R_{\text{st}} < R_{\text{break}}$, with larger mass-size coefficients have larger virial parameters (Fig. 11 d). Additional investigation will be required into the role of pressure in the scale dependent behaviour of α_{vir} , such as the analysis proposed by Krumholz et al. (2025).

5.5. Magnetic fields and gravitational stability in MBM12

From the analysis of ideal MHD equations, Soler & Hennebelle (2017) showed that perpendicular and parallel alignments between magnetic field orientations and column density structures are attractors in the equations of motion. In strongly magnetized (plasma $\beta \sim 0.1$) gas the transition between these two attractor modes are induced through convergent flows where $\nabla \cdot \mathbf{v} < 0$ (Soler et al. 2013; Soler & Hennebelle 2017). Conver-

gent flows can either be large scale flows or self-gravity which dominates magnetic pressure gradients in molecular clouds (Chen et al. 2016). Observational studies of ten Gould Belt regions with *Planck* dust emission and polarisation measurements found a transition column density $N_{\parallel \rightarrow \perp}(\text{H}) = 5 \times 10^{21} \text{ cm}^{-2}$ (Planck Collaboration et al. 2016). This transition $N(\text{H})$ is close to the $N_{\text{c} \rightarrow \text{pl}}(\text{H}) = 10^{21} \text{ cm}^{-2}$ where the upper limits of magnetic field strengths from Zeeman measurements transition from constant to power law (Crutcher 2012; Soler & Hennebelle 2017). The connection between the $N_{\parallel \rightarrow \perp}$ to $N_{\text{c} \rightarrow \text{pl}}(\text{H})$ may indicate a shared mechanism of super-critical filaments between these two transitions. However, this interpretation is weakened by the large scatter in measured $N_{\parallel \rightarrow \perp}(\text{H})$, which ranges from $2 \times 10^{21} \text{ cm}^{-2}$ to $23 \times 10^{21} \text{ cm}^{-2}$, or many clouds not displaying a transition at all (Planck Collaboration et al. 2016; Soler et al. 2017; Carrière et al. 2022b). MBM12 displays a transition column density of $N_{\parallel \rightarrow \perp}(\text{H}_2) \sim 4.5 \times 10^{21} \text{ cm}^{-2}$ and $\alpha \approx 3$ in the Horseshoe. Our virial parameter ignores contributions from internal magnetic pressure or external thermal pressure, which brings up the question of whether the magnetic field is supporting MBM12 from collapse. For a single source, a parallel to perpendicular transition is difficult to interpret (Sect. 6.1.3 of Pattle et al. 2023). The presence of the relative orientation transition indicates the presence of strong magnetic fields $\beta < 1$, convergent velocity flows and possibly super-Alfvénic gas motions. The south of MBM12 Horseshoe would therefore be a candidate for higher resolution kinematic follow-up, to assess whether there are signs of infall or gravitational collapse.

6. Conclusion

We report large-scale ^{12}CO and ^{13}CO ($J = 1 - 0$) line observations of MBM12 with the TRAO radio telescope combined with *Herschel* and *Planck* column density estimates. For the first time in MBM12, we combined an analysis of molecular gas properties ($N(\text{H}_2)$, $X(\text{CO})$, $N(\text{CO})$, $[\text{CO}/\text{H}_2]$), dynamics (multi-scale virial parameters α_{vir}) and magnetic fields (with histogram of relative orientations).

1. We estimated the spatial variation in the molecular gas fraction and 1200 GHz dust opacity, with $\langle \kappa_{1200} \rangle = (192 \pm 7) \times 10^{-3} \text{ cm}^2 \text{ g}^{-1}$, resulting in column densities that range from $2 \times 10^{20} \text{ cm}^{-2}$ to $1.3 \times 10^{22} \text{ cm}^{-2}$.
2. The average CO-to- H_2 conversion factors were $X(^{12}\text{CO}) = 2 \times 10^{20} \text{ cm}^{-2} (\text{K km s}^{-1})^{-1}$ and $X(^{13}\text{CO}) = 7.8 \times 10^{20} \text{ cm}^{-2} (\text{K km s}^{-1})^{-1}$ with significant variation across the field. The average $X(^{12}\text{CO})$ value in MBM12 is equal to the galactic average. We decomposed the $X(\text{CO})$ PDFs into lognormal and power law components, with the power law slopes of $X(^{12}\text{CO}) = -1.21 \pm 0.03$ and $X(^{13}\text{CO}) = -0.78 \pm 0.04$. Future work will investigate the parameters which influence the statistical intracloud behaviour of $X(\text{CO})$.
3. We estimated the CO column density $N(\text{CO})$, and the CO abundances $[\text{CO}/\text{H}_2]$. We incorporated variable $^{12}\text{CO}/^{13}\text{CO}$ isotope ratios calibrated by simulations. We measured $N(\text{CO})$ ranging from $1 \times 10^{16} \text{ cm}^{-2}$ to $1 \times 10^{18} \text{ cm}^{-2}$. The abundances $[\text{CO}/\text{H}_2]$ ranged from 0.9×10^{-5} to 1×10^{-4} with an average of 5.9×10^{-5} .
4. We used dendrograms to calculate multi-scale virial parameters α_{vir} for MBM12. For the Horseshoe and North Compact subregions, for most structures $\alpha_{\text{vir}} \approx 3$ at scales of 0.05–1 pc with masses scaling $M \propto R^2$ and Larson scaling $\sigma_v \propto R^{0.5}$. On the other hand for the North Diffuse and Bow regions $\alpha_{\text{vir}} \approx 8$ at scales of 0.05–1 pc. The Horseshoe has a mass-radius scaling coefficient three times larger than the other subregions, indicating an order of magnitude stronger external pressure on the Horseshoe, compared to the other subregions. Scale dependent α_{vir} measurements can highlight the role of external pressure in regulating star formation molecular clouds.
5. We estimated the histogram of relative orientations in MBM12, and found column density structures parallel to the magnetic field orientation for $N(\text{H}_2) < 4.5 \times 10^{21} \text{ cm}^{-2}$, and some perpendicular structures thereafter. Perpendicular structures were only detected in the south of the Horseshoe subregion, and may indicate the presence of strong magnetic fields and convergent velocity flows.

Our first case study of MBM12 in the B-FROST survey highlights the complementary value of tracing environment, dynamics and magnetic fields. We also stress the value of empirical κ_v calibration for H_2 column densities and assumptions about LTE and isotope ratios for CO column densities. The multi-tracer approach in MBM12 enables comparative studies of low- vs high-mass star formation under varying conditions of turbulence, feedback, and magnetization in large scale molecular cloud surveys.

Acknowledgements. We thank Quentin Remy for supplying the opacity maps of anti-centre clouds. JMV and MJ acknowledge support from the Academy of Finland grant No 348342. EM is funded by the University of Helsinki doctoral school in particle physics and universe sciences (PAPU). VMP acknowledges financial support by the grant PID2020-115892GB-I00, funded by MCIN/AEI/10.13039/501100011033 and by the grant CEX2019-000918-M funded by MCIN/AEI/10.13039/501100011033. VMP gratefully acknowledges also financial support from the European Research Council via the ERC Synergy Grant "ECOGAL" (project ID 855130). DA acknowledges NU FD-CRGP No201223FD8821. We acknowledge the use of data provided by the Centre d'Analyse de Données Etendues (CADE), a service of IRAP-UPS/CNRS (<http://cade.irap.omp.eu>, Paradis et al. 2012). C.W.L is supported by the Basic Science Research Program through the NRF funded by the Ministry of Education, Science and Technology (grant No. NRF-2019R1A2C1010851) and by the Korea Astronomy and Space Science Institute grant funded by the Korea government (MSIT; project No. 2025-1-841-02). This research made use of astrodendro, a Python package to compute dendrograms of Astronomical data (<http://www.dendrograms.org/>). This work made use of Astropy:⁶ a community-developed core Python package and an ecosystem of tools and resources for astronomy (Astropy Collaboration et al. 2013, 2018, 2022).

References

- Alves, J. F., Lada, C. J., & Lada, E. A. 2001, *Nature*, 409, 159
 André, P., Men'shchikov, A., Bontemps, S., et al. 2010, *A&A*, 518, L102
 Arzoumanian, D., André, P., Könyves, V., et al. 2019, *A&A*, 621, A42
 Arzoumanian, D., Furuya, R. S., Hasegawa, T., et al. 2021, *A&A*, 647, A78
 Astropy Collaboration, Price-Whelan, A. M., Lim, P. L., et al. 2022, *apj*, 935, 167
 Astropy Collaboration, Price-Whelan, A. M., Sipőcz, B. M., et al. 2018, *AJ*, 156, 123
 Astropy Collaboration, Robitaille, T. P., Tollerud, E. J., et al. 2013, *A&A*, 558, A33
 Ballesteros-Paredes, J. 2006, *MNRAS*, 372, 443
 Beckwith, S. V. W., Sargent, A. I., Chini, R. S., & Guesten, R. 1990, *AJ*, 99, 924
 Bendo, G. J., Griffin, M. J., Bock, J. J., et al. 2013, *MNRAS*, 433, 3062
 Bertoldi, F. & McKee, C. F. 1992, *ApJ*, 395, 140
 Bohlin, R. C., Savage, B. D., & Drake, J. F. 1978, *ApJ*, 224, 132
 Bolatto, A. D., Wolfire, M., & Leroy, A. K. 2013, *ARA&A*, 51, 207
 Burgh, E. B., France, K., & McCandliss, S. R. 2007, *ApJ*, 658, 446
 Cardelli, J. A., Clayton, G. C., & Mathis, J. S. 1989, *ApJ*, 345, 245
 Carrière, J. S., Ferrière, K., Ristorcelli, I., & Montier, L. 2022b, *A&A*, 668, A42
 Carrière, J. S., Montier, L., Ferrière, K., & Ristorcelli, I. 2022a, *A&A*, 668, A41
 Chen, C.-Y., King, P. K., & Li, Z.-Y. 2016, *ApJ*, 829, 84
 Chevance, M., Krumholz, M. R., McLeod, A. F., et al. 2023, in *Astronomical Society of the Pacific Conference Series*, Vol. 534, Protostars and Planets VII, ed. S. Inutsuka, Y. Aikawa, T. Muto, K. Tomida, & M. Tamura, 1
 Chieze, J. P. 1987, *A&A*, 171, 225

⁶ <http://www.astropy.org>

- Cotten, D. L. & Magnani, L. 2013, *MNRAS*, 436, 1152
- Crutcher, R. M. 2012, *ARA&A*, 50, 29
- Crutcher, R. M., Wandelt, B., Heiles, C., Falgarone, E., & Troland, T. H. 2010, *ApJ*, 725, 466
- Dame, T. M., Hartmann, D., & Thaddeus, P. 2001, *ApJ*, 547, 792
- Dib, S., Kim, J., Vázquez-Semadeni, E., Burkert, A., & Shadmehri, M. 2007, *ApJ*, 661, 262
- Dobbs, C. L., Krumholz, M. R., Ballesteros-Paredes, J., et al. 2014, in *Protostars and Planets VI*, ed. H. Beuther, R. S. Klessen, C. P. Dullemond, & T. Henning, 3–26
- Friesen, R. K., Bourke, T. L., Di Francesco, J., Gutermuth, R., & Myers, P. C. 2016, *ApJ*, 833, 204
- Friesen, R. K. & Jarvis, E. 2024, *ApJ*, 969, 70
- Glover, S. C. O., Federrath, C., Mac Low, M.-M., & Klessen, R. S. 2010, *MNRAS*, 404, 2
- Gómez, J. F., Trapero, J., Pascual, S., et al. 2000, *MNRAS*, 314, 743
- Gong, M., Ostriker, E. C., & Kim, C.-G. 2018, *ApJ*, 858, 16
- Goodman, A. A., Pineda, J. E., & Schnee, S. L. 2009, *ApJ*, 692, 91
- Griffin, M. J., Abergel, A., Abreu, A., et al. 2010, *A&A*, 518, L3
- Hasenberger, B., Lombardi, M., Alves, J., et al. 2018, *A&A*, 620, A24
- Heiderman, A., Evans, II, N. J., Allen, L. E., Huard, T., & Heyer, M. 2010, *ApJ*, 723, 1019
- Hennebelle, P. & Falgarone, E. 2012, *A&A Rev.*, 20, 55
- Hensley, B. S. & Draine, B. T. 2023, *ApJ*, 948, 55
- HI4PI Collaboration, Ben Bekhti, N., Flöer, L., et al. 2016, *A&A*, 594, A116
- Hildebrand, R. H. 1983, *QJRAS*, 24, 267
- Hogerheijde, M. R., Jayawardhana, R., Johnstone, D., Blake, G. A., & Kessler, J. E. 2002, *AJ*, 124, 3387
- Hwang, J., Pattle, K., Lee, C. W., et al. 2025, *ApJ*, 985, 222
- Jeong, I.-G., Kang, H., Jung, J., et al. 2019, *Journal of Korean Astronomical Society*, 52, 227
- Juvela, M. & Montillaud, J. 2016, *A&A*, 585, A38
- Juvela, M., Ristorcelli, I., Marshall, D. J., et al. 2015, *A&A*, 584, A93
- Juvela, M., Ristorcelli, I., Montier, L. A., et al. 2010, *A&A*, 518, L93
- Juvela, M., Ristorcelli, I., Pelkonen, V. M., et al. 2011, *A&A*, 527, A111
- Kauffmann, J., Pillai, T., & Goldsmith, P. F. 2013, *ApJ*, 779, 185
- Kim, J.-G., Ostriker, E. C., & Filippova, N. 2021, *ApJ*, 911, 128
- Kim, M. J., Kim, S., Youn, S., et al. 2012, *ApJ*, 746, 11
- Koch, E. W., Rosolowsky, E. W., Boyden, R. D., et al. 2019, *AJ*, 158, 1
- Kong, S., Lada, C. J., Lada, E. A., et al. 2015, *ApJ*, 805, 58
- Krumholz, M. R., Lada, C. J., & Forbrich, J. 2025, *The Open Journal of Astrophysics*, 8, 91
- Lada, C. J., Lada, E. A., Clemens, D. P., & Bally, J. 1994, *ApJ*, 429, 694
- Ladjele, B., André, P., Könyves, V., et al. 2020, *A&A*, 638, A74
- Lamarre, J. M., Puget, J. L., Ade, P. A. R., et al. 2010, *A&A*, 520, A9
- Lee, J., Saur, A., Mac Low, M.-M., & Li, H. 2025, *ApJ*, 988, 266
- Leroy, A. K., Sun, J., Meidt, S., et al. 2025, *ApJ*, 985, 14
- Levrier, F., Le Petit, F., Hennebelle, P., et al. 2012, *A&A*, 544, A22
- Lewis, J. A., Lada, C. J., Bieging, J., et al. 2021, *ApJ*, 908, 76
- Lewis, J. A., Lada, C. J., & Dame, T. M. 2022, *ApJ*, 931, 9
- Li, G.-X., Wyrowski, F., Menten, K., Megeath, T., & Shi, X. 2015, *A&A*, 578, A97
- Lis, D. C. & Goldsmith, P. F. 1989, *ApJ*, 337, 704
- Liszt, H. S. & Pety, J. 2012, *A&A*, 541, A58
- Liszt, H. S., Pety, J., & Lucas, R. 2010, *A&A*, 518, A45
- Liu, T., Wu, Y., & Zhang, H. 2013, *ApJ*, 775, L2
- Lombardi, M. 2009, *A&A*, 493, 735
- Lombardi, M. & Alves, J. 2001, *A&A*, 377, 1023
- Lombardi, M., Alves, J., & Lada, C. J. 2006, *A&A*, 454, 781
- Lombardi, M., Bouy, H., Alves, J., & Lada, C. J. 2014, *A&A*, 566, A45
- Luhman, K. L. 2001, *ApJ*, 560, 287
- Luo, A.-X., Liu, H.-L., Li, G.-X., Pan, S., & Yang, D.-T. 2024, *Research in Astronomy and Astrophysics*, 24, 065003
- Luo, G., Zhang, Z.-Y., Bisbas, T. G., et al. 2023, *ApJ*, 942, 101
- Magnani, L., Blitz, L., & Mundy, L. 1985, *ApJ*, 295, 402
- Magnani, L., Blitz, L., & Wouterloot, J. G. A. 1988, *ApJ*, 326, 909
- Magnani, L., Onello, J. S., Adams, N. G., Hartmann, D., & Thaddeus, P. 1998, *ApJ*, 504, 290
- McKee, C. F. & Holliman, II, J. H. 1999, *ApJ*, 522, 313
- McKee, C. F. & Tan, J. C. 2003, *ApJ*, 585, 850
- Meeus, G., Juhász, A., Henning, T., et al. 2009, *A&A*, 497, 379
- Miville-Deschênes, M.-A., Murray, N., & Lee, E. J. 2017, *ApJ*, 834, 57
- Montier, L., Plaszczynski, S., Levrier, F., et al. 2015, *A&A*, 574, A135
- Montillaud, J., Juvela, M., Rivera-Ingraham, A., et al. 2015, *A&A*, 584, A92
- Mooney, T. J. & Solomon, P. M. 1988, *ApJ*, 334, L51
- Moriarty-Schieven, G. H., Wannier, & P. G. 1997, *ApJ*, 475, 642
- Nguyen, H., Dawson, J. R., Miville-Deschênes, M. A., et al. 2018, *ApJ*, 862, 49
- Oakes, E. K., Faesi, C. M., Rosolowsky, E., et al. 2025, *ApJ*, 993, 193
- Offner, S. S. R., Taylor, J., Markey, C., et al. 2022, *MNRAS*, 517, 885
- Padoan, P., Juvela, M., Bally, J., & Nordlund, Å. 2000, *ApJ*, 529, 259
- Padoan, P., Pan, L., Juvela, M., Haugbølle, T., & Nordlund, Å. 2020, *ApJ*, 900, 82
- Panopoulou, G. V., Tassis, K., Goldsmith, P. F., & Heyer, M. H. 2014, *MNRAS*, 444, 2507
- Paradis, D., Dobashi, K., Shimoikura, T., et al. 2012, *A&A*, 543, A103
- Pattle, K., Fissel, L., Tahani, M., Liu, T., & Ntormousi, E. 2023, in *Astronomical Society of the Pacific Conference Series*, Vol. 534, *Protostars and Planets VII*, ed. S. Inutsuka, Y. Aikawa, T. Muto, K. Tomida, & M. Tamura, 193
- Pety, J., Guzmán, V. V., Orkisz, J. H., et al. 2017, *A&A*, 599, A98
- Pineda, J. E., Caselli, P., & Goodman, A. A. 2008, *ApJ*, 679, 481
- Pineda, J. L., Goldsmith, P. F., Chapman, N., et al. 2010, *ApJ*, 721, 686
- Planck Collaboration, Abergel, A., Ade, P. A. R., et al. 2014a, *A&A*, 571, A11
- Planck Collaboration, Abergel, A., Ade, P. A. R., et al. 2014b, *A&A*, 566, A55
- Planck Collaboration, Ade, P. A. R., Aghanim, N., et al. 2016, *A&A*, 586, A138
- Pound, M. W., Bania, T. M., & Wilson, R. W. 1990, *ApJ*, 351, 165
- Reach, W. T., Heiles, C., & Bernard, J.-P. 2015, *ApJ*, 811, 118
- Remy, Q., Grenier, I. A., Marshall, D. J., & Casandjian, J. M. 2017, *A&A*, 601, A78
- Roman-Duval, J., Jackson, J. M., Heyer, M., Rathborne, J., & Simon, R. 2010, *ApJ*, 723, 492
- Rosolowsky, E. W., Pineda, J. E., Kauffmann, J., & Goodman, A. A. 2008, *ApJ*, 679, 1338
- Roueff, A., Gerin, M., Gratier, P., et al. 2021, *A&A*, 645, A26
- Santa-Maria, M. G., Goicoechea, J. R., Pety, J., et al. 2023, *A&A*, 679, A4
- Schinnerer, E. & Leroy, A. K. 2024, *ARA&A*, 62, 369
- Shetty, R., Glover, S. C., Dullemond, C. P., et al. 2011, *MNRAS*, 415, 3253
- Singh, A., Matzner, C. D., Friesen, R. K., et al. 2021, *ApJ*, 922, 87
- Skrutskie, M. F., Schneider, S. E., Stiening, R., et al. 1997, in *Astrophysics and Space Science Library*, Vol. 210, *The Impact of Large Scale Near-IR Sky Surveys*, ed. F. Garzon, N. Epchtein, A. Omont, B. Burton, & P. Persi, 25
- Soler, J. D. 2019, *A&A*, 629, A96
- Soler, J. D., Ade, P. A. R., Angilè, F. E., et al. 2017, *A&A*, 603, A64
- Soler, J. D. & Hennebelle, P. 2017, *A&A*, 607, A2
- Soler, J. D., Hennebelle, P., Martin, P. G., et al. 2013, *ApJ*, 774, 128
- Solomon, P. M., Rivolo, A. R., Barrett, J., & Yahil, A. 1987, *ApJ*, 319, 730
- Stark, A. A., Penzias, A. A., & Beckman, B. 1983, in *Surveys of the Southern Galaxy: Proceedings of a Workshop Held at the Leiden Observatory, The Netherlands, August 4–6, 1982*, Springer, 189–194
- Suin, P., Arzoumanian, D., Zavagno, A., & Hennebelle, P. 2025, *A&A*, 698, A119
- Sun, J., Leroy, A. K., Schrupa, A., et al. 2018, *ApJ*, 860, 172
- Szűcs, L., Glover, S. C. O., & Klessen, R. S. 2014, *MNRAS*, 445, 4055
- Szűcs, L., Glover, S. C. O., & Klessen, R. S. 2016, *MNRAS*, 460, 82
- van Dishoeck, E. F. & Black, J. H. 1988, *ApJ*, 334, 771
- van Dishoeck, E. F., Black, J. H., Phillips, T. G., & Gredel, R. 1991, *ApJ*, 366, 141
- Vázquez-Semadeni, E., Palau, A., Ballesteros-Paredes, J., Gómez, G. C., & Zamora-Avilés, M. 2019, *MNRAS*, 490, 3061
- Wilson, R. W., Jefferts, K. B., & Penzias, A. A. 1970, *ApJ*, 161, L43
- Xu, F., Wu, Y., Liu, T., et al. 2021, *ApJ*, 920, 103
- Ysard, N., Jones, A. P., Guillet, V., et al. 2024, *A&A*, 684, A34
- Ysard, N., Köhler, M., Jones, A., et al. 2015, *A&A*, 577, A110
- Zhou, C., Vastel, C., Montillaud, J., et al. 2022, *A&A*, 658, A131
- Zucker, C., Alves, J., Goodman, A., Meingast, S., & Galli, P. 2023, in *Astronomical Society of the Pacific Conference Series*, Vol. 534, *Protostars and Planets VII*, ed. S. Inutsuka, Y. Aikawa, T. Muto, K. Tomida, & M. Tamura, 43
- Zucker, C., Speagle, J. S., Schlafly, E. F., et al. 2019, *ApJ*, 879, 125

Appendix A: Polarisation angles

We derived the plane-of-sky magnetic field (\mathbf{B}_{pos}) orientation angle, ψ_B , from linear polarisation components Q and U using

$$\psi_B = \frac{1}{2} \arctan\left(\frac{U}{Q}\right) \pm 90^\circ, \quad (\text{A.1})$$

which corresponds to the linear polarisation position angle rotated by 90° , and where \arctan is the two-argument arctangent function defined from -180° to $+180^\circ$. Following Montier et al. (2015), we computed the uncertainty in the linear polarisation position angle, σ_{ψ_B} using

$$\sigma_{\psi_B} = \frac{1}{2} \sqrt{\frac{Q^2\sigma_U^2 + U^2\sigma_Q^2 - 2QU\sigma_{QU}}{(Q^2 + U^2)^2}}, \quad (\text{A.2})$$

with σ_Q and σ_U the respective uncertainties in Q and U , and σ_{QU} the covariance of Q and U . We adopt the IAU convention, where the linear polarisation position angle increases from Galactic north to the east (opposite to the Healpix convention requiring the flipping of the sign of U in data taken from the *Planck* Legacy Archive). There is a 180° ambiguity when estimating ψ_B from linear polarisation that only gives the magnetic field orientation. However, it is irrelevant in the study of relative orientations, thus we can define ψ_B in the range $[-90^\circ, +90^\circ]$ from Eq. (A.1) by choosing the sign in the last term accordingly.

Appendix B: Spatial variation in line ratios

We plotted the average spectrum of both isotopologues for rectangular regions in MBM12 in Fig. B.1. The ^{12}CO integrated intensity is shown in the background. The gridlines indicate the regions that were averaged. We also showed the mean $^{12}\text{CO}/^{13}\text{CO}$ line ratio in each region.

Appendix C: Molecular gas fraction

The total hydrogen content along the line of sight $N(\text{H})$ can be decomposed into ionized, atomic and molecular components:

$$N(\text{H}) = N(\text{H}^+) + N(\text{HI}) + 2N(\text{H}_2) \quad (\text{C.1})$$

that implies the molecular fraction f_{mol} is given by:

$$f_{\text{mol}} = 1 - \frac{N(\text{HI}) + N(\text{H}^+)}{N(\text{H})} \quad (\text{C.2})$$

with the molecular hydrogen column density given by

$$N(\text{H}_2) = \frac{f_{\text{mol}}}{2} N(\text{H}) \quad (\text{C.3})$$

We estimated the spatial variation in f_{mol} in MBM12 by combining total column density $N(\text{H})$ estimates from extinction with HI4PI all sky $N(\text{HI})$ estimates (HI4PI Collaboration et al. 2016). We assumed $N(\text{H}^+)$ to be negligible. Figure C.1 shows $N(\text{H})$, $N(\text{HI})$ and f_{mol} at $5'$ resolution. There is a shell of atomic hydrogen across the whole the east side of MBM12. The molecular gas fraction varies between 0.5 and 0.8 on subparsec scales.

Appendix D: Dust opacity determination

The dust opacity can be parameterized as:

$$\kappa_\nu = \kappa_0 \left(\frac{\nu}{\nu_0}\right)^\beta, \quad (\text{D.1})$$

with ν_0 a reference frequency, β a power-law index, and κ_0 the dust opacity at the reference frequency. The values of κ_0 and β are related to dust properties, such as composition, porosity, and size distribution. In Table 2 we summarize ways that the dust opacity at $250 \mu\text{m}$ κ_{1200} can be estimated. Estimates 1 and 2 consist of assuming a relevant literature value of κ_0 at ν_0 with a power law exponent β for Eq. D.1. The range of consequent values in κ_{1200} originates from variation in β . The second class of κ_{1200} estimates is to have a calibrator $N(\text{H})$ to calculate source-specific κ_{1200} . Estimate 3 is the average κ_{1200} for the twelve molecular clouds in the survey of (Lewis et al. 2022), calibrated with extinction. The uncertainties are the standard deviation within the twelve fields, while the range is determined by varying the β of 353 GHz to 1200 GHz. Estimate 4 is the average and range of the surveyed values of $\tau(250 \mu\text{m})/\tau(J)$ from Juvela et al. (2015), with the extinction to $N(\text{H})$ conversion used in Sect. 3.1, without accounting for f_{mol} . Estimate 5 is also based on a calibrated $N(\text{H})$, but instead of extinction, is based on a linear model of multi-wavelength observations of anti-centre clouds, including MBM12 (γ -rays, CO, FIR emission, HI, Remy et al. 2017). They constructed wide-field $40^\circ \times 40^\circ$ maps at 0.175° resolution by linear modeling of HI, CO and free-free emission against a combination of *Planck* τ_{353} and Fermi-LAT γ -ray observations. One can calculate the dust opacity per nucleon $\sigma_\nu = \kappa_\nu \mu_{\text{H}} m_{\text{p}}$ from the Remy et al. (2017) $N(\text{H})$ map. In Fig. D.1 we show an example of the estimate of κ_{1200} by Eq. 3 with $N(\text{H}_2)_{\text{cal}}$ in the case of $f_{\text{mol}} = 1$. Fig. D.2 shows the spatial variations in the dust opacity per nucleon, σ_{353} , compared to the Hildebrand (1983) for $\beta = 2$. The value is close to unity at the edges of MBM12, but with a change of a factor of two within the cloud. Estimate 6 is the values we estimated in Sect. 3.1 of this work.

Appendix E: Image segmentation with $X(\text{CO})$

We fit the $X(\text{CO})$ PDFs with a lognormal distribution, given by

$$f_{\text{LN}}(X(\text{CO})) = \frac{A_{\text{LN}}}{X(\text{CO})\sigma_{\text{LN}}\sqrt{2\pi}} \exp\left(-\frac{(\ln[X(\text{CO})] - \mu_{\text{LN}})^2}{2\sigma_{\text{LN}}^2}\right) \quad (\text{E.1})$$

and with a truncated powerlaw

$$f_{\text{PL}} = A_{\text{PL}} X(\text{CO})^{\alpha_{\text{PL}}} \quad (\text{E.2})$$

where $X(\text{CO})$ was in units of X_{Gal} . The fitted parameters for MBM12 are shown in Tab. E.1. After this PDF decomposition, we investigated whether the statistical modes of the $X(\text{CO})$ PDF may correspond to different physical conditions. We generated binary masks according to whether the PDF is lognormal (LN), powerlaw (PL) or in the excess region (EX), according to these criteria

We estimated the spatial variation in f_{mol} in MBM12 by combining total column density $N(\text{H})$ estimates from extinction with HI4PI all sky $N(\text{HI})$ estimates (HI4PI Collaboration et al. 2016). We assumed $N(\text{H}^+)$ to be negligible. Figure C.1 shows $N(\text{H})$, $N(\text{HI})$ and f_{mol} at $5'$ resolution. There is a shell of atomic hydrogen across the whole the east side of MBM12. The molecular gas fraction varies between 0.5 and 0.8 on subparsec scales.

$$\text{Mask (l,b)} = \begin{cases} \text{LN} & \text{if } X(\text{CO}) \leq X_{\text{LNMax}} \\ \text{PL} & \text{if } X_{\text{LNMax}} < X(\text{CO}) \leq X_{\text{PLMax}} \\ \text{EX} & \text{if } X(\text{CO}) > X_{\text{PLMax}} \end{cases} \quad (\text{E.3})$$

where $X_{\text{LNMax}} = X_{\text{LNMode}} \cdot \exp(1.1775 \cdot \sigma_{\text{LN}})$ where $X_{\text{LNMode}} = \exp(\mu_{\text{LN}} - \sigma_{\text{LN}}^2)$ is the distribution peak of a lognormal. The 1.1775 factor is half the FWHM of a lognormal in log-log space.

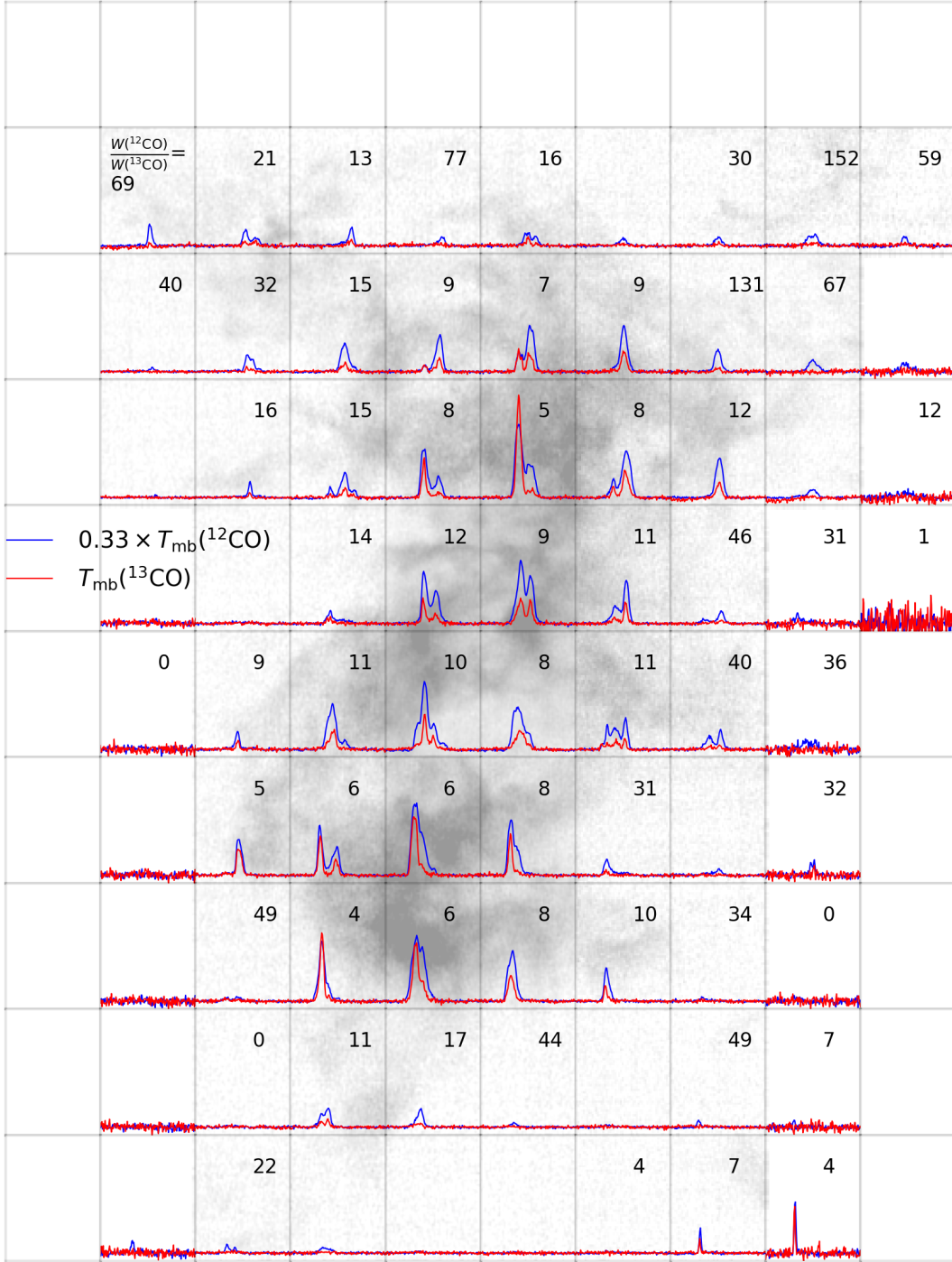


Fig. B.1. Spatial variation in ^{12}CO and ^{13}CO emission (blue and red respectively). The background is the ^{12}CO integrated intensity. Each square shows the mean spectra within each grid position. The $W(^{12}\text{CO})/W(^{13}\text{CO})$ line ratio for $> 3\sigma_{\text{rms}}$ emission is shown in black. Note that $T_{\text{mb}}(^{12}\text{CO})$ has been multiplied by 0.33. Large line ratios > 50 are seen when ^{12}CO is detected but almost no ^{13}CO .

Table E.1. Fitted parameters on the $X(\text{CO})$ PDFs in MBM12 (Fig. 7 and Eqs. E.1 and E.2).

ID	PDF Quantity	A_{LN} (Counts)	μ_{LN} ($\ln[X_{\text{Gal}}]$)	σ_{LN} ($\ln[X_{\text{Gal}}]$)	A_{PL} (Counts)	α_{PL}	PL Range (X_{Gal})
1	$X(^{12}\text{CO})$	1358 ± 32	-0.17 ± 0.01	0.32 ± 0.01	1907 ± 35	-1.21 ± 0.03	[1.0, 10.0]
2	$X(^{13}\text{CO})$	3757 ± 100	1.71 ± 0.01	0.37 ± 0.01	2573 ± 217	-0.78 ± 0.04	[6.5, 20.0]

Notes. The PL Range column shows the $X(\text{CO})$ ranges used for the truncated power law fit.

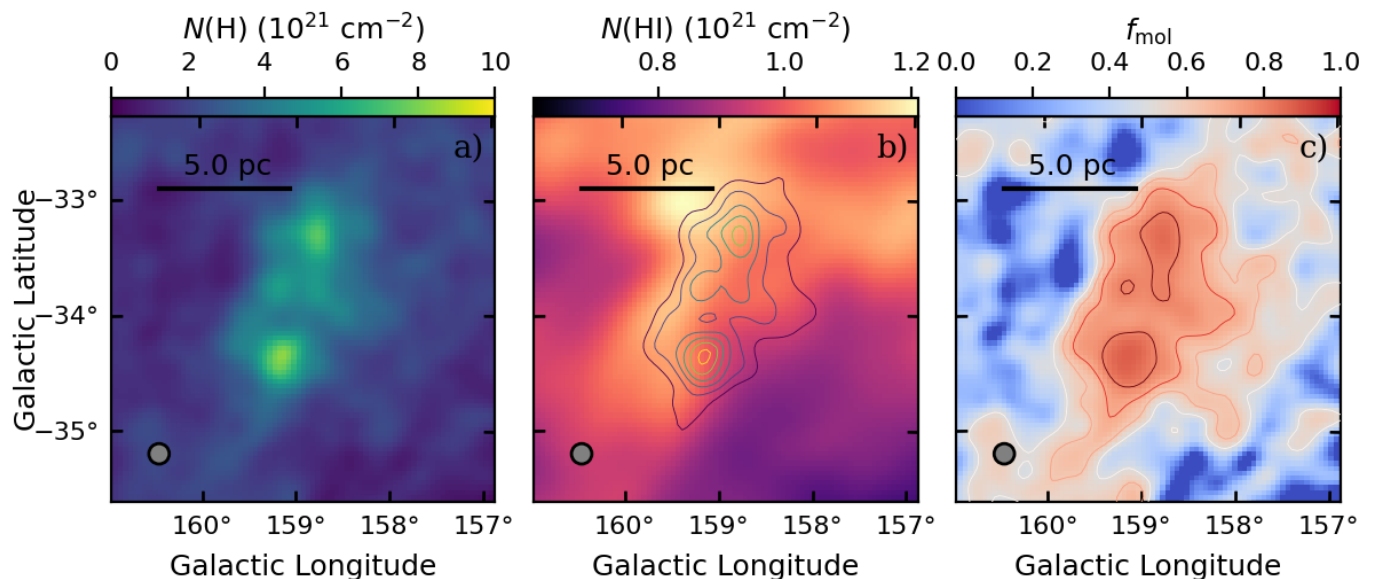


Fig. C.1. Estimate of molecular gas fraction in MBM12. Panel a shows total hydrogen column density from NICEST extinction maps. Panel b shows the atomic hydrogen column density from HI4PI Collaboration et al. (2016). Contours of $N(\text{H}) = [3, 4, 5, 6, 7, 8] \times 10^{21} \text{ cm}^{-2}$ are shown in green. Panel c shows the molecular gas fraction from the combination of these observations with contours of $f_{\text{mol}} = [0.5, 0.6, 0.7, 0.8]$.

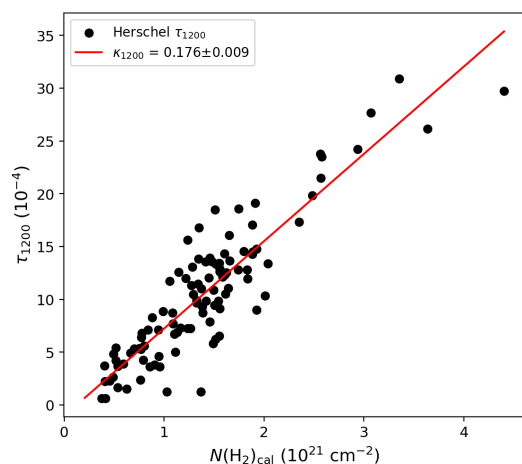


Fig. D.1. Dust opacity estimate at 1200 GHz for MBM12 using the column densities $N(\text{H}_2)_{\text{cal}}$ of Remy et al. (2017) as a calibrator in the case of a molecular gas fraction f_{mol} of 1. The resulting dust opacity is shown.

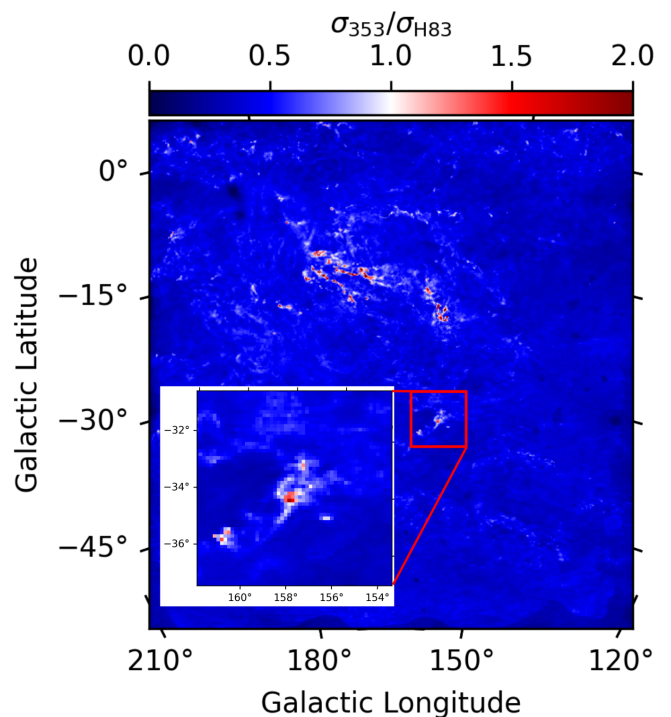


Fig. D.2. Dust opacity per nucleon, σ_v , from multi-wavelength modelling for anti-centre fields from Remy et al. (2017) as a ratio of the commonly used dust opacity from Hildebrand (1983), with $\beta = 2$. The insert is a zoom-in of MBM12, with the same colourscale.

The value of X_{PLMax} is the maximum of the PL Range column of Tab. E.1, just before the excess peak (Fig. 7). Figures E.1 a and e show the three masks for the two isotopologues. We also plotted the histograms of $N(\text{H}_2)$, $N(\text{CO})$ and $[\text{CO}/\text{H}_2]$ for these regions (panels b–d and f–h for ^{12}CO and ^{13}CO respectively). Regarding the maps we note that the EX mask is always at the edge of the cloud. For ^{13}CO it follows the order of EX \rightarrow PL \rightarrow LN from outside to inside the cloud. However, for ^{12}CO , there is a filamentary structure on the inside that is PL, which is not seen in ^{13}CO . This is likely related to ^{12}CO transitioning to high optical depths, while ^{13}CO is still optically thin. The $N(\text{CO})$ PDFs are very different between masks. The LN mask in both isotopologue has a broad lognormal distribution centred around 10^{17} cm^{-2} , while the PL mask is bimodal for ^{12}CO and single peaked for ^{13}CO . The EX mask has the lowest peak value for both isotopologues. The abundance PDFs show mostly lognormal distri-

butions, with a possible powerlaw at the low abundance end for ^{12}CO , while for ^{13}CO the three distributions are lognormal, with the peak abundance decreasing in the order LN \rightarrow PL \rightarrow EX. We consider these masks to segment the MBM12 map into distinct physical regions based on CO chemistry and optical depth effects. The detailed reasons why $X(\text{CO})$ change in these statistical

behaviour requires additional investigation over multiple clouds and other spectral lines. Comparison with radiative transfer and chemistry simulations will also be helpful.

Appendix F: Considerations when interpreting α_{vir}

Most forms of the observational α_{vir} for molecular clouds are the ratio of internal kinetic energy to gravitational energy (e.g. Bertoldi & McKee 1992). There has been an ever-evolving discussion on the (ir)relevance of virial parameters. One's interpretation of α_{vir} varies based on whether one assumes static or dynamic MCs. Forty years ago, it was common to conclude that molecular clouds are in virial equilibrium from the Larson $\sigma_v \propto R^{0.5}$ scaling relation, and to use that to calculate the cloud virial mass (Solomon et al. 1987; Mooney & Solomon 1988; Lis & Goldsmith 1989). From similar static assumptions, some have interpreted $\alpha_{\text{vir}} < 1$ as a sign of other supporting forces such as internal turbulence or magnetic fields (Bertoldi & McKee 1992; Kauffmann et al. 2013). Those discussed above used an assumption of virial equilibrium to either calculate masses or infer some unmeasured force. For the dynamic assumption of MCs, the value of α_{vir} can be used as a measure of (un)boundedness of a cloud. There the assumption is that internal kinetic and gravitational energies are the only relevant energies, and so $\alpha_{\text{vir}} > 1 - 2$ can be used as a simple binary measure for gravitational boundedness. Many users of this approach do flag its tentative nature (Rosolowsky et al. 2008; Friesen et al. 2016; Friesen & Jarvis 2024; Oakes et al. 2025). Strictly speaking, this approach in particular has no way to distinguish if the cloud is gravitationally collapsing (no supporting forces), in pressure equilibrium (unobserved supporting forces), dispersing (unobserved forces stronger than gravity) or fragmenting (Chieze 1987). Virial parameters are a local measure and ignore external pressure, large-scale velocity gradients, and rotation (Ballesteros-Paredes 2006; Chevance et al. 2023). There are also observational biasing effects, such as background subtraction, sampling due to line excitation and variable emission-to-mass conversion factors that may lead to artificially small α_{vir} (Singh et al. 2021). Some have therefore proposed alternative observational estimators of gravitational stability (Li et al. 2015; Krumholz et al. 2025). The observational virial parameter from PPV cubes is different from a 3D virial parameter in a simulation due to projection. In simulations, one can directly calculate gravitational, kinetic and magnetic energies. Some simulations of MCs suggest that observational virial parameters are not associated with cloud stability at all, due to tidal and projection effects (Dib et al. 2007; Kim et al. 2021; Offner et al. 2022; Lee et al. 2025). These considerations show that one should be upfront about assumptions when doing virial analysis, and that the conclusions from a virial analysis alone are only tentative without combination with independent measures.

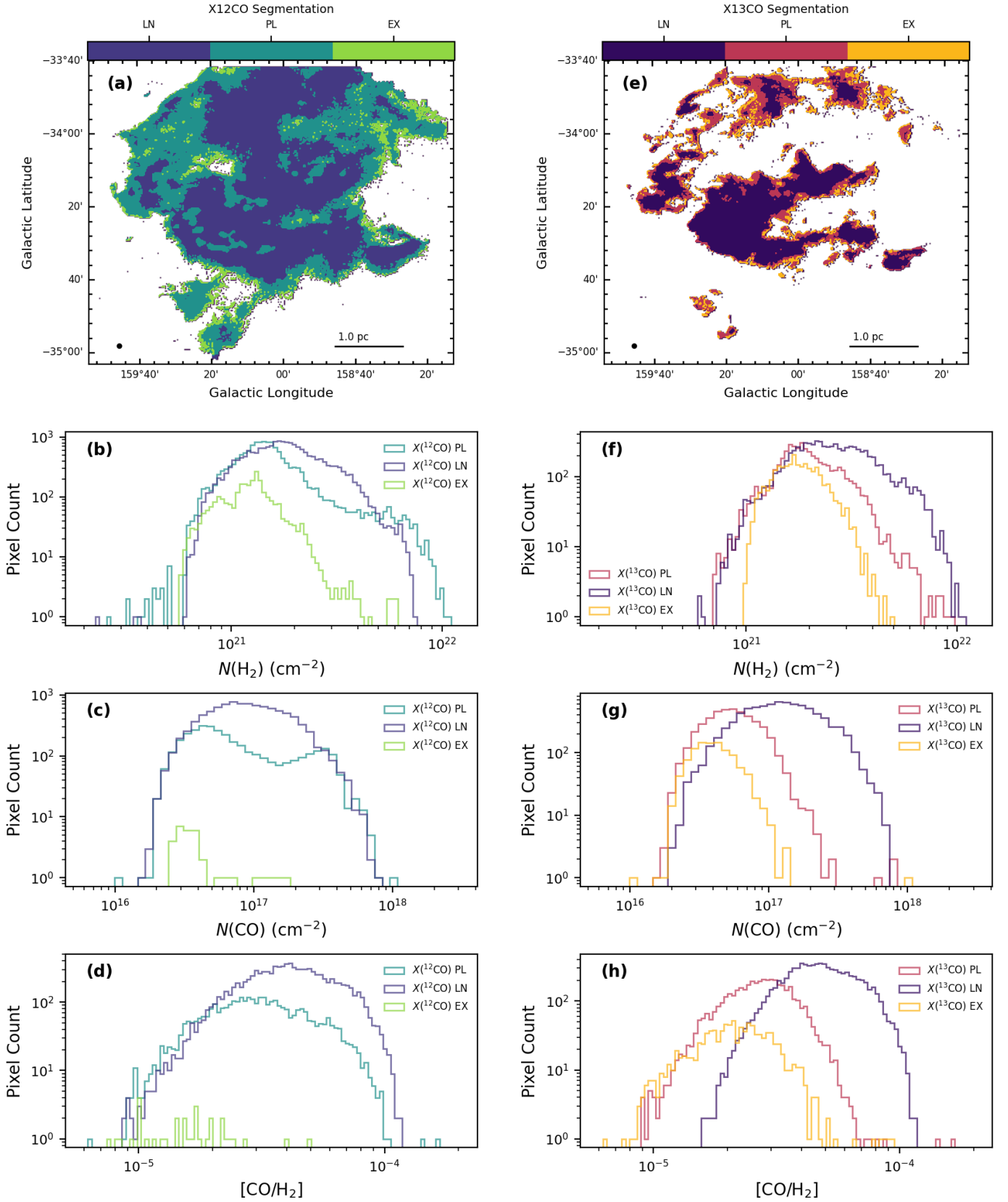


Fig. E.1. Single-isotopologue segmentation of MBM12 based on $X(\text{CO})$ PDF decomposition. Top panels: Spatial distribution of lognormal (LN, left) and power-law (PL, right) classified regions for ^{12}CO (panels a–d) and ^{13}CO (panels e–h), overlaid on the $N(\text{H}_2)$ map. The excess (EX) regions appear predominantly at cloud edges. Lower panels: Histograms of $N(\text{H}_2)$, $N(\text{CO})$, and $[\text{CO}/\text{H}_2]$ for pixels in each classification